Preparing for Success

Searching for a Heavy Non-$q\bar{q}$ Meson in $\Upsilon(6S)$ Decays at Belle II

Shanette De La Motte

Master of Science Candidate
School of Physics
The University of Melbourne
Victoria 3010

Under the Supervision of
Professor Geoffrey Taylor

Thesis submitted October 20th 2017, in partial requirement to the *Master of Science (Physics)*

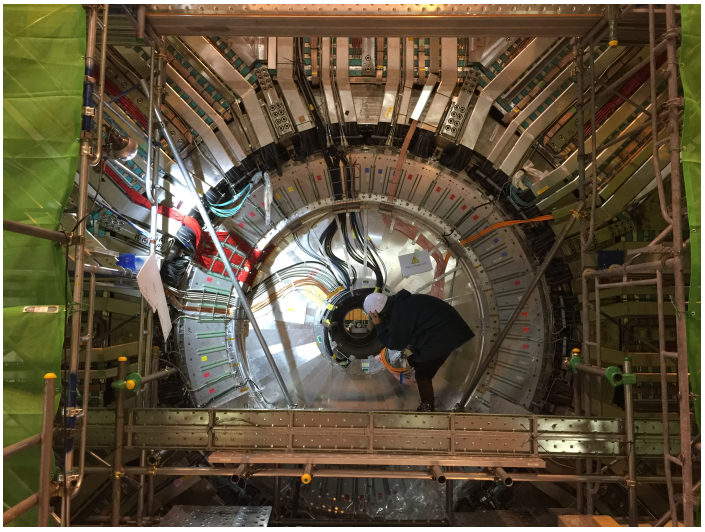

The author 'looking' for exotic physics at the Belle II Detector, Japan. February 2017.

Abstract

While $q\bar{q}$ mesons and qqq baryons are ubiquitous in particle physics, the higher order $qq\bar{q}\bar{q}$ mesons and $qqqq\bar{q}$ baryons are rarely seen, despite being completely allowed by quantum chromodynamics. In 2016, an analysis using data collected with the Belle detector at the KEKB asymmetric e^+e^- collider found evidence for a $qq\bar{q}\bar{q}$ meson of 10610 MeV, referred to as $Z_b^+(10610)$, in $\Upsilon(6S)$ decays. We perform an MC analysis of $\Upsilon(6S) \to [Z_b^+(10610) \to \pi^+ h_b(1P)]\pi^-$ and relevant continuum events to assess how to best see this $qq\bar{q}\bar{q}$ candidate in the upcoming sequel experiment, Belle II. We are able to measure the Z_b^+ using pion recoil mass distributions within error of the recorded invariant mass, for both Phase II and Phase III of Belle II detector geometries. We also improve upon the continuum suppression techniques implemented in the 2016 analysis, first by implementing a better selection criterion based on Fox-Wolfram moment, R2, and secondly by using TMVA toolkit to consider a set of continuum suppression selection criteria.

Statement of Originality

Chapter 1 is a review of relevant exotic QCD literature and previous exotic experiments.
Chapter 2 is a review of the Belle II Detector, based on design reports and letters of intent.
Chapter 3, 4 and 5 contain an original analysis based on MC created by the Belle II Collaboration.

Acknowledgements

It takes a village to raise a child. This thesis is a reflection not only of my efforts, but of those who have supported me.
Firstly, to Professor Geoff Taylor, for taking me under his wing as my Masters supervisor. Thanks for the scotch and fountain pen advice. Dr. Phill Urquijo's generous experimental intuition has also been invaluable to this analysis
Secondly, to my hermaño, Rob "Boston Rob" Muñoz. You're the best thing to come out of Queensland, I'm so glad to have shared a supervisor with you.
Thirdly, to Cate Macqueen. You are a fantastic physicist and my physics life better for having you in it. I want to be you when I grow up
My page count does not allow for me to name every member of Shanette Village, but the largest amount of thanks goes to Scott Williams. His support was comprehensive over the two years of this Masters degree, whether it be bringing raisin toast when I couldn't bring myself to cook, a lift home on when I was lazy, or every single time he forced me out of bed. It was with his support that I succeed in completing this thesis. Also, thanks to him for building layer 3 of the SVD.

Chapter 1

Introduction

The quark model was born of the need for a elegant and compact description of matter. At the beginning of the 1960s, the increasing sophistication in accelerator physics led to the discovery of an enormous number of new particles, beyond the known atomic constituents of electrons, protons and neutrons. Physicists famously doubted that such independence of such a large set of particles, but struggled to reconcile this with a self consistent theory.

Both Murray Gell-Mann and George Zweig are indepdentally credited for the quark model in 1964. [1][2]. This formalism treated the newly discovered particles as composite, made of spin-1/2, point-like particles now known as *quarks*. Common properties between the newly discovered particles could now be explained as similarities in quark components. With the quark model, mesons and baryons were prescribed a quark-based meaning that was consistent with their previously defined spin-statistics and baryon numbers. Leptons remained fundamental, while mesons and baryons were *hadronic*, consisting of a quark-antiquark pair or quark triplet, respectively. This drastically reduced the number of degrees of freedom in massive particles and the similarities between them could now be explained in terms of their underlying quark content.

While the $q\bar{q}$ mesons and qqq baryon models proposed have since been heavily supported by experiment, it is less known $qq\bar{q}\bar{q}$ and $qqqq\bar{q}$ quark groupings were also introduced by Gell-Mann. Referred to as *exotic hadrons*, these states possess spin and baryon number consistent with an abstracted definition of meson and baryon. Despite the fact that Gell-Man's 50 year old inception requires no newer physics than what was proposed in the quark model, the exotic hadrons are rarely seen experimentally.

QUARKS		
	Spin-1/2	
Flavour	*Mass*[MeV]	*Electric charge*
u	2.3	2/3
d	4.8	-1/3
c	1275	2/3
s	95	-1/3
t	160000	2/3
b	4180	-1/3

LEPTONS		
	Spin-1/2	
Flavour	*Mass*[MeV]	*Electric charge*
e	0.510999	-1
ν_e	0	0
μ	105.658	-1
ν_μ	0	0
τ	1776.82	-1
ν_τ	0	0

Figure 1.1: Table of fundamental fermions[3]. Quarks have both colour and electric charge, while a lepton's electric charge is negative or neutral, with no colour. As fundamental particles, they are pointlike and thus below the wavelength of visible light. The term 'colour' is merely a label.

This thesis will construct an analysis, based on the simulation of an upcoming particle physics experiment, to shed light on the previously seen $qq\bar{q}\bar{q}$ meson candidate, $Z_b^+(10610)$. If confirmed, this particle will stand as a blatant example of a non-$q\bar{q}$ meson and motivate the high energy physics community to address a long unanswered question; *if exotic hadrons are to exist with the same physics as generic ones, why have decades of high energy experiments observed almost exclusively 2 and 3-quark hadrons, leaving higher order hadrons relatively unseen?*

MESONS		
Spin-0		
	Mass[MeV]	*Structure*
η	547.86	$\frac{1}{\sqrt{6}}(u\bar{u}+d\bar{d}-2s\bar{s})$
π^+	139.57	$u\bar{d}$
π^-	139.57	$\bar{u}d$
π^0	134.98	$\frac{1}{\sqrt{2}}(u\bar{u}-d\bar{d})$
K^+	493.677	$u\bar{s}$
K^-	493.677	$\bar{u}s$
K^0	497.614	$d\bar{s}$
$\overline{K^0}$	497.614	$\bar{d}s$

BARYONS		
Spin-1/2		
	Mass[GeV]	*Structure*
Λ	1.115683	uds
p	1.007276	uud
n	1.008665	udd
Ξ^0	1.31486	uss
Ξ^-	1.32171	dss
Σ^+	1.18937	uus
Σ^-	1.18937	dds
Σ^0	1.192642	uds

BARYONS		
Spin-3/2		
	Mass[GeV]	*Structure*
Ω^-	1.672	sss
Ξ^{*-}	1.535	dss
Ξ^{*0}	1.532	uss
Σ^{*-}	1.383	dds
Σ^{*0}	1.384	uds
Σ^{*+}	1.387	uus
Δ^-	1.232	ddd
Δ^0	1.232	udd
Δ^+	1.232	uud
Δ^{++}	1.232	uuu

Figure 1.2: Table of hadrons. It was once sufficient to class particles by their spin(fermionic or bosonic) and the Greek term for the approximate mass symmetry they belonged to; *leptós*,*mesós*, *baryós* or small, intermediate and large. These terms were redefined within the quark model.

1.1 Hadronic Substructure: Quantum Chromodynamics

To appreciate the structure of exotic hadrons, it is important review the structure of conventional hadrons . Quantum Chromodynamics (QCD) is the Quantum Field Theory (QFT) that describes the internal binding forces and structure of hadrons, in terms of their constituent quarks. QCD was motivated by the existence of the spin-3/2 Ω_s^- baryon, whose $s_\uparrow s_\uparrow s_\uparrow$ composition seemingly required three s quarks in the exact same quantum state. As fermions, this was forbidden by the Pauli Exclusion Principle and a new quantum number was invoked to demarcate the three s quarks: the *colour charge*. Each s quark was assigned a colour charge, alongside it's electric charge; the charges are referred to as *red*, *blue* and *green*. The existence of 3 charges is one of the key features that lead to the complexity of QCD.

As a subgroup of the Standard Model(SM) formalism, QCD shares some behaviours with the other two underlying gauge theories, Quantum Electrodynamics (QED) and the weak interaction. It's *gauge bosons* are a set of 8 massless spin-1 *gluons*, which mediate the interaction between particles that possesses the QCD conserved charge, the aforementioned colour charge. It's dynamics are referred to as the *strong force* named after it's strength over the electric force in short-range quark interactions.

Exploring the mathematics that underpin QCD emphasises it's peculiarities as a SM gauge group. The requirement of 3 charges (rather than 1, as per QED and the weak interaction) leads to an $SU(3)$ group structure. To achieve a colour neutral state, quarks can combine with equal proportions of all colour charges to form a traditional baryon $q^r q^b q^g$. They may also combine with *antiquarks*, their antiparticles which possess the opposing "anti-color" quantum number to form a traditional meson $q^c \bar{q}^{\bar{c}}$, where $c \in \{r, b, g\}$, with anticolour implied . As the $SU(3)$ group is also non-Abelian, QCD has an octet of gauge bosons that hold the group charges themselves, as outlined in Figure 1.3.

Due to the aforementioned differences between the other SM subgroups, QCD exhibits two unique phenomena: *colour confinement* and *asymptotic freedom*. These are results of the energy-dependent strong coupling in contrasting regimes; the gluon potential is strongly confining of colour-charges as the energy is lowered, while at increasing energies the coupling is expected to asymptotically approach zero. Thus, quarks and gluons are restricted to colour neutral combinations; all searches for unbound quarks and gluons having null results[3]. At much higher energies however, such as that of the early universe, the strong coupling is diminished enough to allow for a "quark-gluon plasma" state.

GLUONS *Spin-1*	
λ_a	*Colour state*
λ_1	$\frac{1}{\sqrt{2}}(R\bar{B}+\bar{R}B)$
λ_2	$\frac{i}{\sqrt{2}}(R\bar{B}-\bar{R}B)$
λ_3	$\frac{1}{\sqrt{2}}(R\bar{R}-\bar{B}B)$
λ_4	$\frac{1}{\sqrt{2}}(G\bar{R}+\bar{G}R)$
λ_5	$\frac{i}{\sqrt{2}}(R\bar{G}-\bar{R}G)$
λ_6	$\frac{1}{\sqrt{2}}(G\bar{B}+\bar{G}B)$
λ_7	$\frac{i}{\sqrt{2}}(B\bar{G}-\bar{B}G)$
λ_8	$\frac{1}{\sqrt{3}}(R\bar{R}+B\bar{B}-2G\bar{G})$

(a)

$$\lambda_1=\begin{bmatrix}0&1&0\\1&0&0\\0&0&0\end{bmatrix}\ \lambda_2=\begin{bmatrix}0&-i&0\\i&0&0\\0&0&0\end{bmatrix}\ \lambda_3=\begin{bmatrix}1&0&0\\0&-1&0\\0&0&0\end{bmatrix}$$

$$\lambda_4=\begin{bmatrix}0&0&1\\0&0&0\\1&0&0\end{bmatrix}\ \lambda_5=\begin{bmatrix}0&0&-i\\0&0&0\\i&0&0\end{bmatrix}\ \lambda_6=\begin{bmatrix}0&0&0\\0&0&1\\0&1&0\end{bmatrix}$$

$$\lambda_7=\begin{bmatrix}0&0&0\\0&0&-i\\0&i&0\end{bmatrix}\ \lambda_8=\frac{1}{\sqrt{3}}\begin{bmatrix}1&0&0\\0&1&0\\0&0&-2\end{bmatrix}$$

(b)

Figure 1.3: List of gluon colour charges, in the Gell-Mann Matrix normalisation. Gluons transform as an octet under SU(3) transformations.

$$\mathcal{L}_{\mathcal{QCD}}=-\tfrac{1}{4}G^i_{\alpha\beta}G_i^{\alpha\beta}+\bar{q}_i(i\gamma^\mu D_\mu-m)_{ij}q_j$$

Figure 1.4: QCD Lagrangian, which describes the dynamics of quarks (q_i). $G^i_{\alpha\beta}$ represents the gluon field strength tensor, $G^i_{\alpha\beta}=\partial_\alpha A^i_\beta-\partial_\beta A^i_\alpha-gf^{ijk}A^j_\alpha A^k_\beta$, with gluon field A^i_β

(a) Quark-quark-gluon (b) Gluon 3-vertex (c) Gluon 4-vertex

Figure 1.5: Vertices allowed by the QCD Lagrangian. As gluons themselves have colour charge, they can also couple to other gluons, unique to QCD.

1.2 Exotic Hadrons and Current Models

With knowledge of the quark-gluon interactions that give rise to standard hadrons, we can now progress to exotic hadrons. The challenge of establishing exotica is two-fold. First, observations of non-$q\bar{q}$ or non-qqq candidates are generally too rare to establish statistical significance. Secondly, with so few statistics, it is difficult to test the numerous theoretical models of their structure. While this thesis will focus on non-$q\bar{q}$ mesons, below we discuss other exotic hadron candidates for completeness. These are sorted according to their theoretical model. The discussion of the Belle Collaboration's contribution to exotic hadrons is reserved for Section 1.3.

1.2.1 Models of non-$q\bar{q}$ Mesons

Both exotic and standard mesons have the following generalised meson properties:

- They have baryon number 0 ($\mathcal{B}=0$)
- Their constituents charged under QCD. Their overall charge sum is colourless.
- They have an even number of quarks (As $\mathcal{B}=\frac{1}{3}(n_q-n_{\bar{q}})=0$ and $n_q+n_{\bar{q}}=n_{tot}\implies n_q=n_{\bar{q}}\implies n_{tot}$ is even)
- They have integer spin ($n_{tot}=n_\uparrow+n_\downarrow$ is even $\implies n_\uparrow-n_\downarrow$ is even $\implies \mathcal{S}=\frac{1}{2}(n_\uparrow-n_\downarrow)$ is an integer)

$$\mathbf{3} \otimes \bar{\mathbf{3}} = \mathbf{1} \oplus \mathbf{8}$$
$$\mathbf{3} \otimes \mathbf{3} \otimes \bar{\mathbf{3}} \otimes \bar{\mathbf{3}} = 2(\mathbf{1}) \oplus 4(\mathbf{8}) \oplus \mathbf{10} \oplus \overline{\mathbf{10}} \oplus \mathbf{27}$$
$$\mathbf{3} \otimes \mathbf{3} \otimes \mathbf{3} \otimes \mathbf{3} \otimes \mathbf{3} \otimes \mathbf{3} = 5(\mathbf{1}) \oplus 16(\mathbf{8}) \oplus 10(\mathbf{10}) \oplus 5(\overline{\mathbf{10}}) \oplus 9(\mathbf{27}) \oplus \mathbf{28} \oplus 5(\mathbf{35})$$
$$\mathbf{3} \otimes \mathbf{3} \otimes \mathbf{3} \otimes \bar{\mathbf{3}} \otimes \bar{\mathbf{3}} \otimes \bar{\mathbf{3}} = 6(\mathbf{1}) \oplus 17(\mathbf{8}) \oplus 7(\mathbf{10}) \oplus 7(\overline{\mathbf{10}}) \oplus 9(\mathbf{27}) \oplus 2(\mathbf{35}) \oplus 2(\overline{\mathbf{35}}) \oplus \mathbf{64}$$

Figure 1.6: Allowable mesons. Quarks transform as triplets (irreducible representation **3**, or $\bar{\mathbf{3}}$ for antiquarks) in SU(3). Taking the direct product of the representations demonstrates which combinations can form mesons, as confinement suggests only colourless (SU(3) irreducible representation **1**) hadrons can propagate.

Mesons with Quarks

Figure 1.6 demonstrates how the states $qq\overline{qq}$, $qqqqq$ and $qqq\overline{qqq}$ classify as exotic mesons. The four-quark state, $qq\overline{qq}$ can be described with one of three models: as a *compact tetraquark*, as *hadroquarkonium* or as a *mesonic molecule* [4].

The compact tetraquark model involves four quarks bound by gluon exchange. More specifically, rather than each quark bound to each of the three other quark, we understand the compact tetraquark to exist due to a gluon exchanged between diquarks and antidiquarks. While a diquark ($\mathbf{3} \otimes \mathbf{3} = \bar{\mathbf{3}} \oplus \mathbf{6}$) and an antidiquark($\bar{\mathbf{3}} \otimes \bar{\mathbf{3}} = \mathbf{3} \oplus \bar{\mathbf{6}}$) do not contain a colour singlet alone, together they build up $[qq]_{\bar{\mathbf{3}}}[\overline{qq}]_{\mathbf{3}} = [qq\overline{qq}]_{\mathbf{1}}$, demonstrated by line 2 of 1.6. The compact tetraquark is a suggested model of some light scalar mesons, such as $f_0(980)$ existing as $\frac{[su][\bar{s}\bar{u}]+[sd][\bar{s}\bar{d}]}{\sqrt{2}}$[5]. Confirming this structure can prove difficult, as sub-GeV mass allows for relativistic mixing, where an $SU(3)$ flavour symmetry may be more pertinent than fixed constituents.

The hadroquarkonium model is inspired by the *quarkonium-like* discoveries in heavy-flavour physics. It is modelled as quarkonium in a "cloud" of light hadronic matter. Exotica such as $Z_c^+(4430)$ may be considered consistent with this model, where it's confirmed minimal quark content $c\bar{c}u\bar{d}$ [6] could be arranged as $\psi(2S)\pi^+$, explaining how it acts as charmonium and acts with electric charge. The quarkonium-excited light hadron bond is thought to be a QCD analogue to the *van der Waals force* of Chemistry, where temporary and localised net colour charges in each hadron that may allow for gluon exchange.

The mesonic molecule model suggests that four-quark states can be made with two $q\bar{q}$ pairs are bound via pseudoscalar mesons. This is a result of the same residual strong force that binds the protons and neutrons in atomic nuclei. This state is inspired by the "baryonic molecule" deuteron, the nucleus of hydrogen-2 isotope. Deuteron consisting of a proton and a neutron thus being the only stable *dibaryon* and a spin-1 hexaquark.

This model is popular in characterising the $Z_b^+(10610)$, the exotic state whose existence will be the focus of this thesis. As will be discussed further in Section 1.3, $Z_b^+(10610)$ decays via the strong force, predominantly to mixture of $B^+\bar{B^{*0}}$ and$B^{*+}\bar{B^{*0}}$[7]. This, as well it's 10610 MeV mass being suspiciously close to the sum of B^+ and B^* suggests that $Z_b^+(10610)$ exists as a molecule of B-mesons.

$$\mathbf{8} \otimes \mathbf{8} = \mathbf{1} \oplus 2(\mathbf{8}) \oplus \mathbf{10} \oplus \overline{\mathbf{10}} \oplus \mathbf{27}$$
$$\mathbf{8} \otimes \mathbf{8} \otimes \mathbf{8} = 2(\mathbf{1}) \oplus 8(\mathbf{8}) \oplus 4(\mathbf{10}) \oplus 4(\overline{\mathbf{10}}) \oplus 6(\mathbf{27}) \oplus 2(\overline{\mathbf{35}}) \oplus \mathbf{64}$$
$$\mathbf{8} \otimes \mathbf{8} \otimes \mathbf{8} \otimes \mathbf{8} = 8(\mathbf{1}) \oplus 32(\mathbf{8}) \oplus 20(\mathbf{10}) \oplus 20(\overline{\mathbf{10}}) \oplus 3(\mathbf{27}) \oplus 2(\mathbf{28}) \oplus 2(\overline{\mathbf{28}}) \oplus 15(\mathbf{35}) \oplus 15(\overline{\mathbf{35}}) \oplus 12(\mathbf{64}) \oplus 3(\mathbf{81}) \oplus 3(\overline{\mathbf{81}}) \oplus \mathbf{125}$$
$$\mathbf{3} \otimes \bar{\mathbf{3}} \otimes \mathbf{8} = \mathbf{1} \oplus 3(\mathbf{8}) \oplus \mathbf{10} \oplus \overline{\mathbf{10}} \oplus \mathbf{27}$$

Figure 1.7: Allowable mesons, with gluon consituents. *Gluons transform as octets (irreducible representation **8**) in SU(3). Colourless (SU(3) irreducible representation **1**) can be obtained as the cross product of any number of gluons, or even as a quark-gluon hybrid.*

Mesons with Gluons

In a departure from the quark model that not even Gell-Mann pondered, QCD permits bound states of all colour charged states, including the gluon. As a gluon posses a sum of colour charges, outlined in Figure 1.3, combination with gluons of opposite colour charges can result in a colour neutral state such as $\mathbf{g}^{r\bar{b}}\mathbf{g}^{\bar{r}b}$ or $\mathbf{g}^{r\bar{b}}\mathbf{g}^{b\bar{g}}\mathbf{g}^{g\bar{r}}$. These states are referred to as *glueballs* and can be labelled as exotic mesons, as the combination of spin-1 bosons gives an integer spin state. Experimentally, a glueball candidate can be demarcated from a conventional meson of the same spin upon inspection of quantum numbers, where a gg glueball can possess $J^{PC} = 0^{++}$, a non-allowed combination for $q\bar{q}$ mesons. The hybrid state, $q\bar{q}g$ is modelled as a $q\bar{q}$ state with persistent gluon, which can also posseses a non allowed quantum number combination, $J^{PC} = 1^{-+}$. The GlueX experiment, a fixed-beam target experiment taking place at Jefferson Lab Virginia, intends to look for persistent gluonic excitations, coupled to quarks as hybrids or as pure glueballs, as suggested by the non-allowed quantum number combinations. [8]

1.2.2 Models of non-qqq Baryons

Both exotic and standard baryons have the following generalised baryon properties.

- They have baryon number 1 ($\mathcal{B} = 1$, or $\mathcal{B} = -1$ for antibaryons)
- They are made of quarks whose charge sum is colourless.
- They have odd number of quarks (As $\mathcal{B} = \frac{1}{3}(n_q - n_{\bar{q}}) = 1$ and $n_q + n_{\bar{q}} = n_{tot} \implies n_q = 3 + n_{\bar{q}}$ and $n_{tot} = 2n_{\bar{q}} + 3$)
- They half-integer spin ($n_{tot} = n_\uparrow + n_\downarrow$ is odd $\implies n_\uparrow - n_\downarrow$ is odd $\implies \mathcal{S} = \frac{1}{2}(n_\uparrow - n_\downarrow)$ is a half-integer)

$$\mathbf{3} \otimes \mathbf{3} \otimes \mathbf{3} = \mathbf{1} \oplus \mathbf{8} \oplus \mathbf{8} \oplus \mathbf{10}$$
$$\mathbf{3} \otimes \mathbf{3} \otimes \mathbf{3} \otimes \mathbf{3} \otimes \bar{\mathbf{3}} = 3(\mathbf{1}) \oplus 8(\mathbf{8}) \oplus 4(\mathbf{10}) \oplus 2(\overline{\mathbf{10}}) \oplus 3(\mathbf{27}) \oplus \mathbf{35}$$

Figure 1.8: Allowable baryons

Pentaquarks

Non-qqq baryons have enjoyed the most recent success. In 2016, the LHCb collaboration published their observation of the existence of the first pentaquarks, occuring as intermediate resonances in $\Lambda_b^0 \to J/\psi p\pi^-$[9] and $\Lambda_b^0 \to J/\psi pK^-$[10]. The resonances, labelled as $P_c^+(4380)$ and $P_c^+(4450)$ achieved statistical significance of 9σ and 12σ respectively, therefore being credited as a discovery. Similar to the explanation of the $Z_b^+(10610)$ composition above, both pentaquarks gave away their constituents via a flavour-conserving strong decay, $P_c(4XXX) \to J/\psi p$, thus consisting of $uudc\bar{c}$. While successful in experiment, it too waits for substructure classification. Pentaquarks can also be modelled as either compact, as a bag of 5 quarks connected gluon exchange, or in a "molecular" arrangements, as a baryon and meson bound by a pseudoscalar exchange.

1.3 Belle's Next Heavy Non-$q\bar{q}$ Meson: $Z_b^+(10610)$

Currently, the most cited paper published by the Belle Collaboration is the first practical evidence of an exotic hadron candidate [11]. Taking place at the the asymmetric energy particle accelerator *KEKB* in Tsukuba,

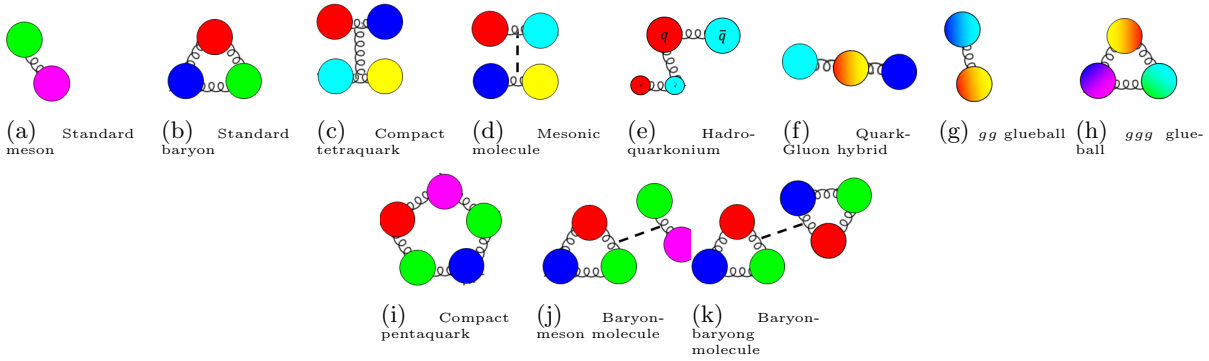

Figure 1.9: Schematics representations of exotic hadrons. *The colour convention is derived from the additive colour method, such that anti-red is represented as cyan, anti-green is represented as magenta and anti-blue is represented as yellow.*

Japan, electron and positrons were collided at centre of mass (COM) energy equivalent $\Upsilon(4S)$ mesons. $\Upsilon(4S)$ is a 10580 MeV $b\bar{b}$ meson with a 96% branching fraction to $B\bar{B}$ pairs. This earned the accelerator the title of *B-factory*, as it was designed to provide a surplus of $B\bar{B}$ charge parity violation (CPV) in charge conjugates pairs, $B\bar{B}$.

Despite having no intention in QCD exotica, the serendipitous 2003 observation of exotica candidate $X(3872)$ was found as an intermediate resonance in $B^{\pm} \to K^{\pm}\pi^{+}\pi^{-}J/\psi$, as $B^{\pm} \to K^{\pm}X(3872)$ and $X(3872) \to \pi^{+}\pi^{-}J/\psi$. Due to the heavy mass of the charm quark, charmonic resonances ($c\bar{c}$ mesons) are non-relativistic and could be easily predicted by considering allowable angular momentum quantum numbers. At the time, charmonium physics consisted of looking for the predicted, but unobserved charmonia that possess these quantum numbers, of which Belle's X(3872) was expected to belong. However, the titular mass of 3872 MeV was not consistent with mass predictions with the allowable spin quantum numbers for $c\bar{c}$ mesons. Deviating further from being characterised as $c\bar{c}$, the sum of D and D^{*} meson masses was within the calculated error on the observed X(3872) mass, as if X(3872) acted as a single meson with the structure of two. It was for this reason that X(3872) was thought to not be a $q\bar{q}$ meson, but a bound state with the same composition as $D\bar{D}^{*}$

The Belle experiment championed the search for exotic mesons, obtaining the first evidence for other 4-quark candidates in its run between 1999 to 2010. Exotica in the heavy-quark sector have proved more lucrative than searches for states such as $\pi\pi$ or the sub-GeV states detailed earlier, whose relativistic behaviour make determining minimum quark content difficult. Heavy exotica candidates at Belle have included $Z_c(3900)$, $Z(4430)$ and the subject of this thesis, the $Z_b^{+}(10610)$ and its higher order version $Z_b^{+}(10650)$. The $Z_b^{+}(106XX)$ states, where the 10610 MeV version has higher statistical significance, is the front runner amongst other non-$q\bar{q}$ candidates. For reasons explained below, it must be bottomonium-like(containing $b\bar{b}$ and mesonic by conservation laws but also exhibit a net charge and isospin. If these attributes truly exist simultaneously in Z_b^{+} mesons, this suggests it's minimal quark content is $u\bar{d}b\bar{b}$.

We intend to construct our own analysis to find $Z_b^{+}(10610)$ in Belle II data, a sequel experiment set to take place with upgrade to the KEKB collider. We first review below the two papers which discuss the methods by which the first observations of this non-$q\bar{q}$ candidate were made.

1.3.1 2011: *Observation of two charged bottomonium-like resonances in* $\Upsilon(5S)$ *Decays*

Further to investigating $\Upsilon(4S) \to B\bar{B}$ during the Belle experiment, physics runs were also conducted at COM energy corresponding to the higher order $\Upsilon(5S)$ resonance, whose larger mass of 10860 MeV was over threshold to decay to and thus measure CPV in $B_s\bar{B_s}$ pairs. However, during such runs, measurements of the branching fraction of $\Upsilon(5S)$ decay equation 1.10a branching fractions were surprisingly two orders of magnitude larger than decays from $\Upsilon(4S)$, suggesting an intermediate decay contribution not present in $\Upsilon(4S)$. This anomaly

motivated investigation into dipion decays of $\Upsilon(5S)$ to lower order $\Upsilon(mS)$, as well opposite parity bottomonium state $h_b(nP)$ shown in equation 1.10b.

$$e^+e^- \to \Upsilon(5S) \to \Upsilon(mS)\pi^+\pi^+ \qquad e^+e^- \to \Upsilon(5S) \to h_b(nP)\pi^+\pi^-$$

(a) For m=1,2,3 (b) For n=1,2

Figure 1.10: $\Upsilon(5S)$ dipion decays of interest. The Z_b^+ resonance was present in both process, as the same mass.

The 2011 analysis looked for exotic contributions by conducting a substructure analysis on $\Upsilon(5S)$ data taken from Belle, consisting of three $\Upsilon(mS)$ and two $h_b(nP)$ decay paths. For Υ path substructure, the method employed was to combine pairs of decay products and evaluate this invariant mass for each event. A true three-body decay would not favour one pairing over another, while any biases in pairing might suggest a two-stage decay with an intermediate resonance. To calculate the required invariant masses, $\Upsilon(mS)\pi^+$ and $\pi^+\pi^-$, directly detected pion energies were simple to apply, while $\Upsilon(mS)$ candidates required a"bottom-up" reconstruction from directly detected muons via $\Upsilon(mS) \to \mu^+\mu^-$. Evaluating the invariant masses for the h_b path is more nebulous, as this bottomonium decays to a photon and η_b, which itself has poorly defined branching ratios. As such, the "top-down" recoil method must be used to consider any intermediate contributions to this path, to calculate $M_{h_b\pi^\pm}$ as explained in fig 1.11.

$$\begin{aligned} P_{e^+} + P_{e^-} &= P_{\Upsilon(5S)} \\ &= P_{h_b(mS)} + P_{\pi^+} + P_{\pi^-} \\ \implies P_{h_b(mS)} + P_{\pi^\pm} &= P_{e^+} + P_{e^-} - P_{\pi^\mp} \\ &= P_{rec,\pi^\mp} \end{aligned}$$

Definition of the four-momentum recoiling from final state particle f, originating from initial particles i

$$P_{rec,f} = \sum_i (P_i) - P_f$$

Figure 1.11: Recoil kinematics: The four-vector (and thus invariant mass) of $h_b\pi^\pm$ can be found from initial beam energies and a second $\pi^\mp$, without reconstructing h_b. The invariant mass associated with $P_{rec,\pi^\mp}$ is called the recoil mass, or $M_{miss,\pi^\mp}$, and is exactly equal to $M_{h_b\pi^\pm}$. The definition of recoil mass is in the right, an important quantity in this thesis.

The results from Figure 1.12 across the 5 channels are consistent with two intermediate resonance, rather than a direct 3 body decay. These twin peaks, which averaged across the 2 h_b paths and 3 Υ paths, have mass $M_1 = 10607.2 \pm 2.0 MeV/c^2, \Gamma_1 = 18.4 \pm 2.4 MeV$ and $M_1 = 10652.2 \pm 1.5 MeV/c^2, \Gamma_1 = 11.5 \pm 2.2 MeV$. Respectively, these were labelled $Z_b(10610)$ and $Z_b(10650)$. The magnitude of the twin peaks exceeded 10σ in statistical significance for all Υ channels, 16σ in $h_b(1P)$ and 5.6σ in $h_b(2P)$. With such uncertainties, this study can be considered the first observation of $Z_b(10610)$ and $Z_b(10650)$ and confirmation of the cascading $\Upsilon(5S) \to Z_b\pi^\pm \to (b\bar{b})\pi^+\pi^-$ decay.

As an intermediate particle in a cascade decay, the quantum numbers of the Z_b resonances are fixed by the $\Upsilon(5S)$ mother particle and the bottomonium and pion final products. Isospin, beauty quantum number ($n_q - n_{\bar{q}}$, where $q = b$), $J-$spin and electric charge are conserved overall, all indicative of a strong decay process. In this way, the Z_b can be deemed to carry isospin and charge opposite to that of its partnered pion, to conserve $Q = 0$ and $I = 0$ of $\Upsilon(5S)$. Therefore, as a spin-1 particle, Z_b could have $(qq\prime)^\pm$ structure, where q must be an isospin-carrying quark, either u or d. However if one instead considers beauty, the decay to h_b suggests $b\bar{b}$ structure. As all bottomonia are strictly $b\bar{b}$, thus chargeless and isospin zero, the aforementioned attributes are not possible within ordinary $q\bar{q}\prime$ mesons. If one however employs the exotic definition of the meson, as the Belle Collaboration concluded, the Z_b could satisfy all results of the cascade decay with at least 4 quarks. A specific quark structure hypothesis was able to be placed on both $Z_b^\pm(10610)$ and $Z_b^\pm(10650)$, due to the coincident invariant mass of $(B^*\bar{B})^\pm$ and $(B^*\bar{B}^*)^\pm$.

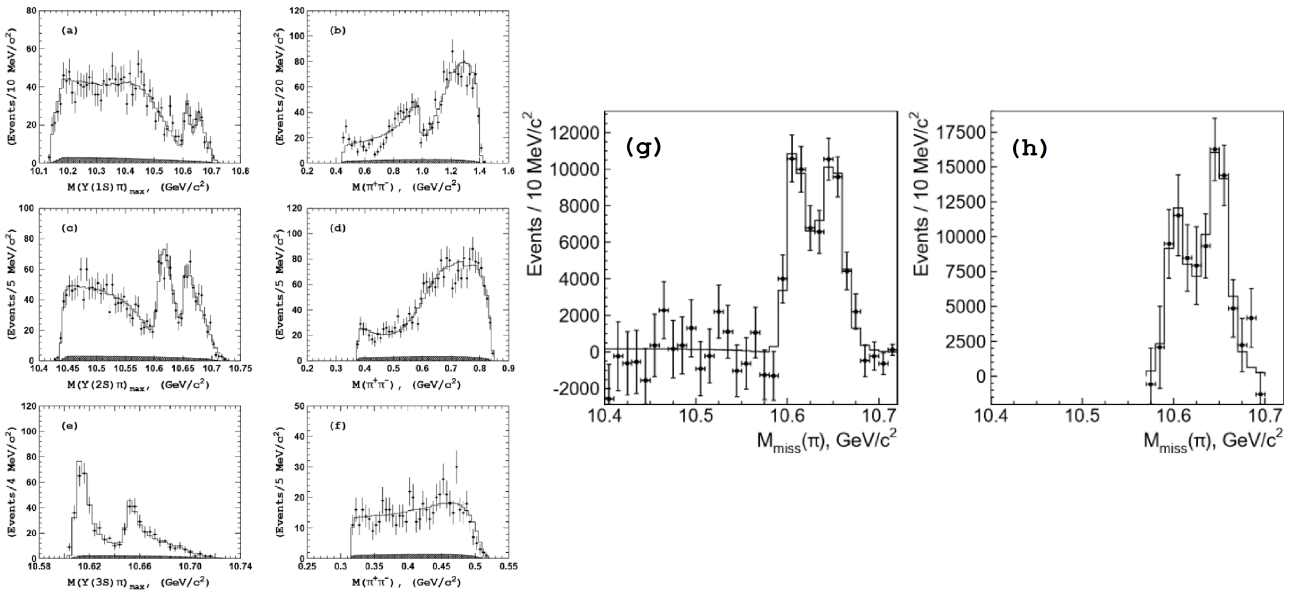

Figure 1.12: Invariant mass fits for $\Upsilon(mS)$ decay path and recoil mass fits for $h_b(nP)$ decay path (adapted from [12]). *Fit results denoted by open histogram, experimental data given as points with error bars. Histograms (a)(b) are of decays to $\Upsilon(1S)$, (c)(d) to $\Upsilon(2S)$ and (e)(f) to $\Upsilon(3S)$, all with background contributions shaded. Histograms (a),(c) and (e) show consistent twin peaks in the vicinity of 10610 MeV and 10650 MeV across all order of m, in product pairing $\Upsilon(mS)\pi$. Histograms (b),(d) and (f) show the distributions of $M_{\pi^+\pi^-}$, with less consistent maxima. Histograms (g)(h) are of pion recoil masses from decays to $h_b(1P)$ and $h_b(2P)$ respectively, with twin peaks consistent with Υ cases.*

$$e^+e^- \to \Upsilon(5S) \to Z_b(106XX)\pi^- \qquad Z_b(106XX) \to \Upsilon(mS)\pi^+$$

(a) For m=1,2,3

$$e^+e^- \to \Upsilon(5S) \to Z_b(106XX)\pi^- \qquad Z_b(106XX) \to h_b(nP)\pi^+$$

(b) For n=1,2

Figure 1.13: $\Upsilon(5S)$ dipion decays of interest, as cascade decays. $Z_b(106XX)$ is either 10610MeV or 10650MeV resonance.

1.3.2 2016: *Energy scan of the* $e^+e^- \to h_b(nP)\pi^+\pi^-$ *(n=1,2) cross sections and evidence for* $\Upsilon(11020)$ *decays into charged bottomonium-like states*

The most recent observation of $Z_b^+(10610)$ was in an analysis of two parts. First, cross sections $e^+e^- \to h_b(nP)\pi^+\pi^-$ was measured at varying energies, with peaks at COM energy 10860 MeV and 11020 MeV. As these are the masses of the $\Upsilon(5S)$ and the next order bottomonium $\Upsilon(6S)$, this agreed with the outcome of the 2011 analysis, that $e^+e^- \to h_b(nP)\pi^+\pi^-$ could take place via $\Upsilon(5S)$. This was also was the first observation of the same process via $\Upsilon(6S)$, motivating the second study into the presence of $Z_b^+(106XX)$ at this new COM energy.

It can be seen that there is very little resolution in the $M_{miss,\pi}$ spectra of Figure 1.14b and Figure 1.14c, when compared to that of the $\Upsilon(5S)$ result in Figures 1.12(g) and 1.12(h). This is a result of the magnitude of the Υ data sets, where 121.4 fb^{-1} of $\Upsilon(5S) \to h_b(nP)\pi^+\pi^-$) was used in 2011, whereas only 1 fb^{-1} was available in the $\Upsilon(6S)$ decay in the 2016 analysis. In particular, there is no visible demarcation between the $Z_b^+(10610)$ and $Z_b^+(10650)$ states and we are thus unable to conclude if both the 10610 MeV and 10650 MeV resonance are present at $\Upsilon(6S)$.

1.4 The Role of this Analysis

As charged, bottomonium-like candidates, the $Z_b(106XX)$ resonances are in blatant opposition to the $q\bar{q}$ defintion. It is imperative to conduct futher measurement of these resonances, so as to identify the true minimum

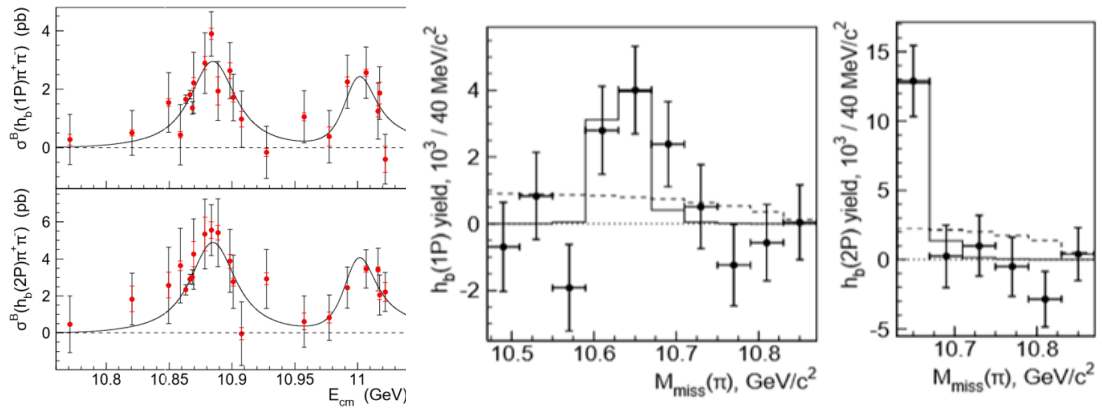

(a) (b) (c)

Figure 1.14: Results from 2016 $Z_b^+(106XX)$ analysis (adapted from [13]). *Figure 1.14a demonstrates that the Born cross section,* $\sigma^B(e^+e^- \to h_b(nP)\pi^+\pi^-)$ *is maximum at the* $\Upsilon(5S)$ *and* $\Upsilon(6S)$ *for both* h_b*. Specifically, as the focus of this thesis,* $\sigma^B(e^+e^- \to h_b(1P)\pi^+\pi^-)$ *is* $2.89 \pm 1.04(stat.) \pm 0.18(corr.syst.) \pm 0.13(uncorr.syst.)$ *around the* $\Upsilon(5S)$ *resonance and* $2.57 \pm 0.88 \pm 0.13 \pm 0.15$ *around the* $\Upsilon(6S)$*. Figure 1.14b and Figure 1.14c demonstrate* $M_{miss,\pi}$ *derived from* $\Upsilon(6S) \to h_b(nP)\pi^+\pi^-)$*.*

quark content. If this is found to be consistent with Gell-Mann's 50 year old hypothesis, QCD will be thrust back into the spotlight. Faced this time with a particle zoo of exotica, theoretical physicists will need to reinvigorate the field of QCD, to accomodate for it's higher order applications to hadronic structure.

It is of particular interest now more than ever to consider an analysis in heavy non-$q\bar{q}$ mesons, as the KEKB collider undergoes the technical upgrade to *SuperKEKB*. The upgraded collider is poised to drastically increase the rate of e^+e^- collisions, thus allowing for a larger number of events in which $Z_b^+(106XX)$ to be produced. As the successor to the original experiment that found first evidence of a number of heavy-quark exotica, the upcoming Belle II experiment is the only B-factory currently able to assess these candidates. While the LHCb experiment has also successfully contributed to five-quark exotica in the heavy sector, we can expect better results with SuperKEKB. The LHCb spectrometer exists within a proton-proton collider, where CMS energy and thus resultant interactions can vary greatly depending on how the proton energy is distributed amongst it's constituents. As a collider of fundamental particles, it is easier to consistently produce collisions of a fixed CMS energy. We can therefore have a higher yield of desired events, in our case at $\Upsilon(6S)$ energy, than at LHCb.

This thesis will contribute to the exotica search at Belle II, by narrowing Belle's analysis to the specific decay channel $\Upsilon(6S) \to \pi^-[Z_b^+(10610) \to h_b(1P)\pi^+]$. From this is point onwards, Z_b^+ will be used strictly in reference to $Z_b^+(10610)$, as $Z_b^+(10650)$ is not considered in this analysis. We will also assume that charge conjugation is implied, such that any mention Z_b^+ also includes Z_b^- originating from $\Upsilon(6S) \to [Z_b^- \to h_b(1P)\pi^-]\pi^+$. Whereas the original Belle experiment only gathered 1 fb^{-1} of data via this channel, we will plan for an analysis of up to 50 fb^{-1}, to improve upon the poorer statistics of the previous Z_b^+ observation. This search can be performed as early as 2018, when SuperKEKB enters into Phase II of comissioning. At this time, it will undergo initial collisions take place with some particle tracking limitations. Phase III, where full data taking can begin is scheduled for 2019 commencement. Thus, it could be within the next 5 years that Belle II could be the pioneering collaboration to confirm the structure of this 4 quark meson.

Chapter 2

SuperKEKB and the Belle II Detector: Hardware of the Belle II Experiment

In contrast to high-energy experiments such as the ATLAS Experiment at CERN, the approach of Belle II is to produce large data samples, in order to conduct high-precision measurements of newly discovered processes. SuperKEKB is poised to improve its luminosity from Belle's $2.11 \times 10^{34} cm^{-2} s^{-1}$ to $80 \times 10^{34} cm^{-2} s^{-1}$, set to become the highest luminosity collider when at peak performance. With emphasis on producing a large data set to pursue rare decays, the experiment is therefore well suited to elucidating the flavour structure of exotic hadrons, such as Z_b^+.

Before beginning our analysis, we will review the method of particle collision and detection planned for the Belle II experiment, particularly in improvements over the original experiment. A full description of this can be found in the Belle II Technical Design Report[14] and the Letters of Intent [15][16][17], as this chapter will summarise the hardware concepts in the context of how we can best detect Z_b^+ when construction is completed.

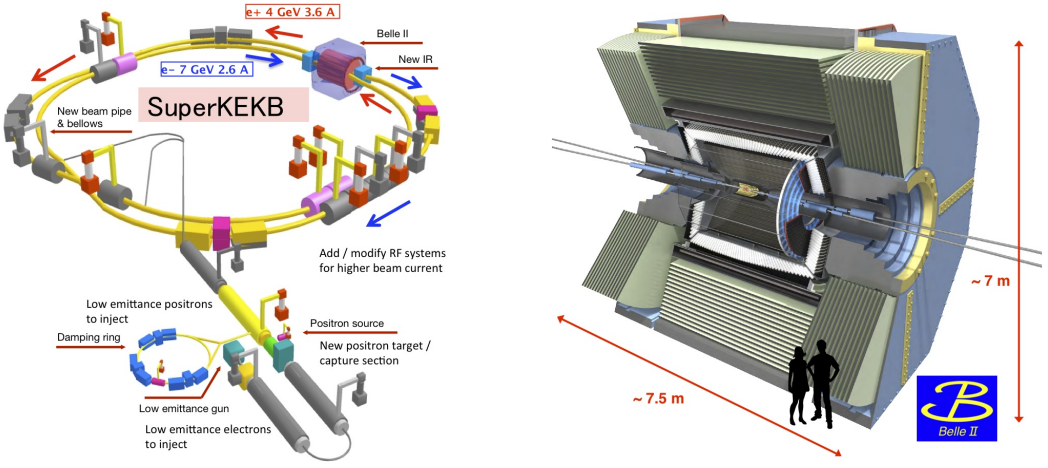

Figure 2.1: Schematics of the SuperKEKB collider and the Belle II Detector.

2.1 The SuperKEKB Collider

The KEK facility, from the Japanese *Kō Enerugī Kasokuki Kenkyū Kikō* or *High Energy Accelerator Research Organization*, is the site of of both the Belle and Belle II experiments. Located in Tsukuba, Japan, the SuperKEKB collider operates on almost the same principles as KEKB, with both designed to collide electrons and positrons at CMS energy to produce B mesons. The new generation B-factory is referred to as a *Super-B*

factory, where implementation of the new *nano-beam scheme* increases the rate of e^+e^- colllisions. This is performed by squeezing the height of the e^+ and e^- beams so that their area of overlap is more compact the Interaction Point (IP).

As an accelerator, SuperKEKB consists of four main sections: an injector linear accelerator, a damping ring, the two counter-propagating storage rings and the interaction point.

- Collider electrons are sourced from the *injector linear accecelerator*, or linac, where they are accelerated to 7 GeV over a 600m straight, by applying a 6.7 MV radio frequency (RF) voltage. Positrons are also produced here as secondary particles in the interaction of other electrons and a tungsten target. The positrons are accelerated to 4 GeV in the linac.
- The nano-beam scheme requires positrons with lower beam energy emittance, so a *damping ring* of 135m radius is used to induce synchrotron radiation. A further RF voltage is applied to accelerate and collimate the beam, minimising emittance.
- The storage rings, or beam lines are of circumference 3016.26 m, with one carrying the electron beam and the other the positron beam. The name Low Energy Ring (or LER) IS the positron beam storage ring and High Energy Ring (or HER) to the electron beam storage. The asymmetry in beam energy is desirable, so as to steer the direction of particle decays for best detection, in this case, the direction of HER. In the case of $\Upsilon(6S)$, electrons are accelerated to 7.29 GeV and positrons to 4.11, to give COM 11.02 GeV.

Particles in the HER and LER can propagate for up to 10 minutes, a large decrease from the hour lifetime of KEKB. This is a sacrifice in the nano-beam scheme, as the compactified IP results in higher rate of intra-beam interactions The momentum of electrons and positrons within the beam can then divert, hit detector materials and create a shower of undesired particles which could be misidentified as the result of an e^+e^- collision. This effect was not present in the original Belle experiment and will become an important part of our analysis, when looking at sources of background events in Chapter 3. Other relevant sources of *beam induced background* are beam-gas scattering, which can take place via bremsstrahlung or Coulomb scattering. A perfect vacuum may not always persist in the interaction region, so that beam particles may scatter off gas particles. In the Coulomb case, electrons and positrons scatter away fromt he collimated beam elastically, or in the case of bremsstrahlung, with the emission of a photon. Both lead to particles that can induce showering in the surrounding materials.

2.2 Subdetector Components of the Belle II Detector

The Belle II Detector is stationed around the interaction region of SuperKEKB, where electron-positron collisions occur in a 20mm diameter, beryllium pipe. The detector is a barrel spectrometer, with subcomponents stacked radially outwards. Particle detection occurs within each subcomponent, with the results of each considered when assigning a particle identity. We will only consider the function of each subdetector relevant to our analysis, in the context of pion particle identification (π-PID) as required by this analysis.

Vertex Detection: The Pixel and Silicon Vertex Detectors

Vertex detection involves determining where the decay of a particle took place. For the Belle II experiment, the detector will contain a pixel detector (PXD) consisting of two layers of sensors located at 14mm and 22mm radially from the beam pipe. The sensors consist of 8 million silicon pixel cells that operate as Depleted Field Effect Transistors (DEPFET). Particles from the IP modulate the electric field running through each transistor, thus registering the location of a hit. allowing for excellent spatial resolution of hits. The PXD is a new addition to the original vertex detector, needed to accomodate for fast detection of the larger number of collisions taking place and to improve the signal-to-noise ratio with the new susceptibility to beam background.

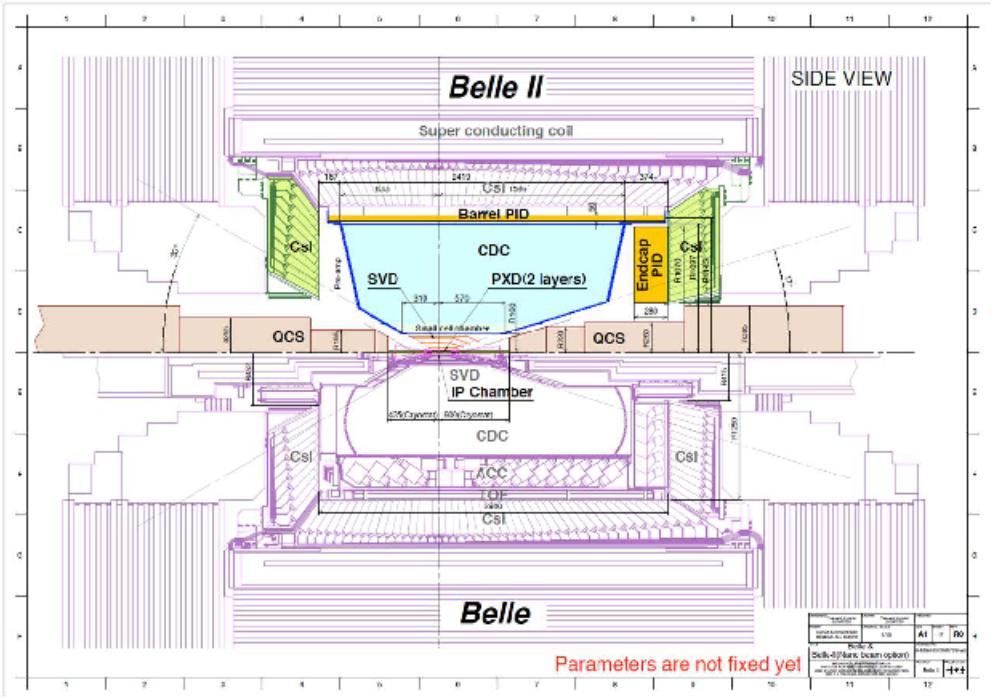

Figure 2.2: Cross-section of the Belle and Belle II Detector, demonstrating the difference in subdetectors. The z-axis is from left to right and theta is measure anti-clockwise from positive z-axis. The detector is barrel in shape, demonstrating azimuthal symmetry in detection.

Vertexing from the PXD is performed in conjunction with the silicon vertex detector (SVD). The SVD has four layers between 3.8 cm and 14.0 cm radially from beam pipe, double the distance seen in Belle. It is capable of detecting particles at polar angles $17^{\circ}<\theta<150^{\circ}$, where the symmetric acceptance accounts for the directional decay production associated with asymmetric beam energy. Each layer is a double-sided silicon strip detector, detecting via induced semiconductor currents, where a hit confidence is enhanced by coinicidence of multiple layered detections. Together, the PXD and SVD allow for high spatial resolution of initial track positions. The variables used in this analysis that depend on vertexing are dr and dz, which are radial distance and z-direction distance of detection respectively. We will accept pions as originating from our desired process, and not from beam background events, if they are measured at dr <0.3cm and dz <2cm.

Central Drift Chamber (CDC)

The CDC is a large cylindrical section that encompasses the vertexing detectors, extending from 16cm to 113cm from the beam pipe. The section is filled with 30 μm diameter wires that run parallel to the cylinder axis and are held at a fixed electric potential. The method by which it detects particles is similar to the function of a smoke alarm; the chamber is filled with a mix of inert helium-ethane gas, which can become ionised by the passage of charged products. Now charged themselves, the gas molecuels "drift" towards and influence the current in the sensor wires, allowing for detection. A 1.5 T magnetic field is present in the chamber, which by the Lorentz force, results in curved trajectories of moving charged particles. This allows for charge-mass ratio of a particle to be identified, by the direction and magnitude of the radius of curvature, $r = \frac{mv}{qB}$. Combination of the initial conditions from the vertexing detctors, the full track of a charged particle in the detector can be reconstructed.

As well as being important in track reconstruction, the CDC can also provides charged particle identification from energy lost per distance in the gaseous medium. The mean energy lost, described by the Bethe-Bloch equation, is a function of relativistic boost of the particle in lab frame $\beta\gamma$. As $\beta\gamma = \frac{p}{m}$, the energy loss in gas is a function of relativistic boost, which can be matched to a characteristic curve for each particle hypothesis of mass m. Depending on this characteristic energy loss, a likelihood quantity $\mathcal{L}_m$ can be assigned to how well a particle matches this hypothesis. For our analysis, we will want to choose particles that are most likely to be pions, over the other charged particles that can be detected, electrons, muons, kaons and protons. We will

accept pions provided that their pion likelihood, $\mathcal{L}_\pi$, is greater than their likelihood of being protons, $\mathcal{L}_p$, or kaons, $\mathcal{L}_K$. Specifically, we would like $(\frac{\mathcal{L}_\pi}{\mathcal{L}_{p/K}})$ >0.1, sometimes implemented as *delta log likelihood*, $\log(\mathcal{L}_\pi)$ - $\log(\mathcal{L}_{p/K}) = \log(\frac{\mathcal{L}_\pi}{\mathcal{L}_{p/K}})$ >log(0.1) . Similarly, the probability that a particle is defined as as an electron, denoted as *PIDe*, is defined as the difference in likelihoods such that $\frac{\mathcal{L}_]}{\mathcal{L}_\pi}$. Electron likelihoods can also be derived from the electronmagnetic calorimeter.

Time-of-Propagation (TOP) Counter

The TOP counter in the Belle II detector is a combination of two machines in the Belle detector, the time-of-flight and aerogel Cherenkov counter. The TOP counter is located on the border of the CDC and contributes to particle identification, especially to delta log likelihood between kaons and pions. Operating on the principle of Cherenkov radiation, where particle may move faster than the speed of light in a medium, thus emitting a characteristic cone of light. Size of this circle subtended by this cone can be used to demarcate between pions and kaons. More over, the time of flight can be measured within the medium, thus combining the two concepts to perform particle identification.

Electromagnetic Calorimeter

The ECL is a detector for QED-interaction particles, specifically photons, electrons and some low energy muons. It is located at 1.25m from the beam line. As a calorimeter, it measures energy deposits of QED particles that interact with it. It consists of a caesium-iodide scintillator crystals, in which QED particles interact with by showering and pair production. The event shape of the shower can be used to demarcate between electrons, photons and muons, which make small deposits if any.

K_L^0-Muon Detector

The KLM is the final subdetector, consisting of alternating iron and detector elements, with the intention of detecting some of the higher momentum final state particles. Specifically these are it's namesake particles, the neutral K_L and μ. Neutral particles, such as the K_L, will not leave tracks in the CDC as they are not charged, so K_L detection is based heavily in KLM, where they can be identified in showering events in matter. However, our analysis looks to the difference in likelihoods between pions and charged pions, so the KLM is not relevant to us.

2.3 Detector Commissioning Schedule

The Belle II Detector has 3 key stages of commissioning. Phase I, which has already taken place, is the detector operating with no particle collisions, so as to calibrate beam currents and measure background events. Phase II features the first particle collisions with all subdetectors, minus the vertexing detectors. Phase III will be a full scale Physics run, where the full suite of subdetectors are implemented. As mentioned previous, the tracking of particle trajectories, momentum and energy can all be measured accurately in the CDC, without the use of vertexing equipment. It will be of interest to see if our analysis can take place with the loss in tracking efficiency associated in Phase II, as Phase II is due to commence as early as 2018. Full vertex detection will not be available until Phase III, scheduled between 2018-2019. If we are able to demonstrate via simulation, that we could accurately identify the presence of $Z_b^+(10610)$ in Phase II, we could be identifying this four-quark candidate as early as next year.

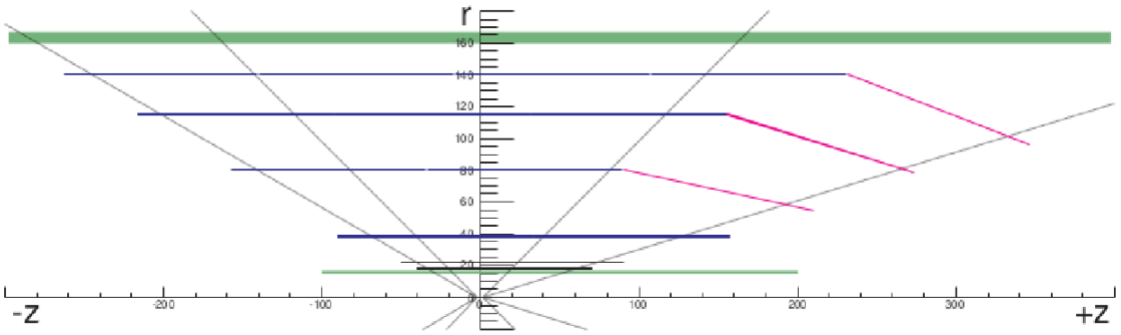

Figure 2.3: Cross-section of the vertex detector system. The first two layers closest to the z-axis are PXD, while the latter 4 layers are SVD. The first SVD layer, referred to as the third VXD layer, was built at The University of Melbourne. Units are in centimetres.

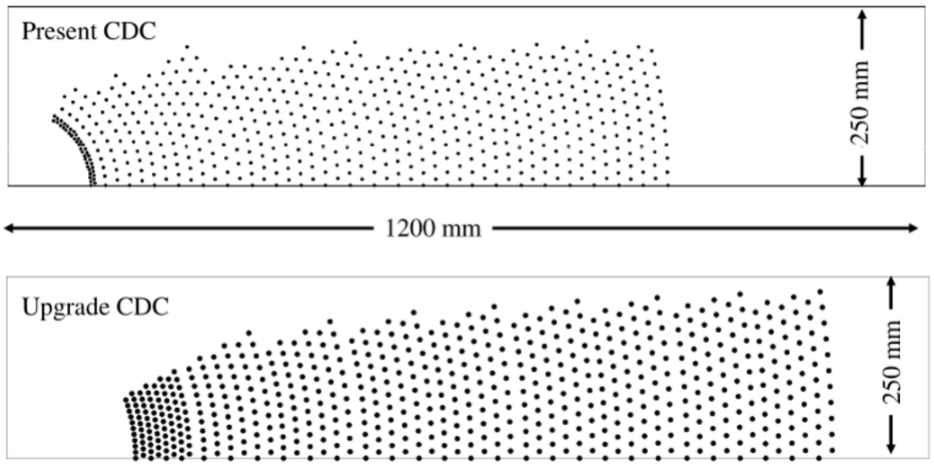

Figure 2.4: Belle CDC (*top*) versus Belle II CDC (*bottom*).

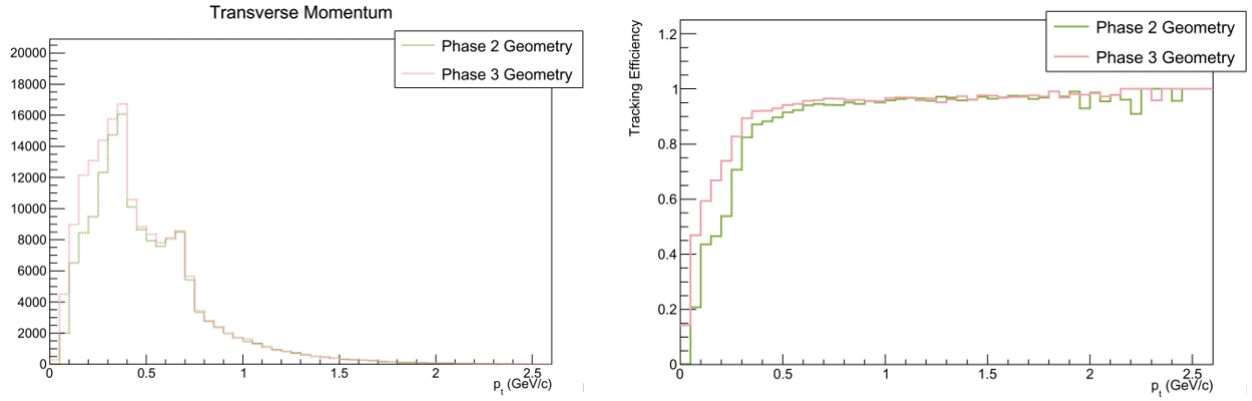

Figure 2.5: Track efficiency and momentum reconstruction, as simulated for Phase II and Phase III detector geometry for pions in our Z_b^+ event. The lime green line indicates Phase II, and we see that for 80% tracking efficiency, we can only resolve pions with transverse momentum 0.3 GeV/c or higher. This is because the lack of vertexing close to the interaction point means that pions must have has sufficient transverse momentum to travel the radial distance to the centra drift chamber. This also will affect our recoil mass distribution of pions that signal Z_b^+, as these will be lower momentum pions. We will see this in the truth MC of Chapter 3.

Chapter 3

Monte Carlo Simulation of Z_b^+ and Background Processes in $\Upsilon(6S)$ Decays

Our discussion so far has consisted of how Z_b^+ was previously measured at the Belle experiment and how future detection would take place after upgrading the accelerator to SuperKEKB. The next step is to assess the feasibility of a Z_b^+ analysis in $\Upsilon(6S)$ decays at Belle II. For this, we use computer-generated e^+e^- collision data in order to study how a Z_b^+ event may present itself when real $\Upsilon(6S)$ data becomes available.

To accurately model high-energy particle interactions, we must consider the indeterminism of quantum observables. Particle decay parameters are stochastic, such that a resultant particle's energy, lifetime, momentum and mass are spontaneously assumed according to calculable probability amplitudes. This can be emulated via the *Monte Carlo* statistical technique, where values are randomly chosen from a given sample space. By repeated calls to Monte Carlo techniques, one can therefore mimic a particle's random choice of kinematic eigenvalues and apply energy conservation to derive results of each decay. Data generated according to this technique will henceforth be referred to as *MC*.

3.1 MC Generation and Analysis Strategy

Generating an MC data set of the magnitude comparable to the Belle II experiment's expected luminosity is not possible for a single analyst. Instead, the Belle II Collaboration has a dedicated data production group with access to high-performance computing, releasing MC to analysis users. The software format is identical to the format of real collision data, meaning that prepared analyses can be applied easily when the true Belle II data set becomes available. An important duty of the Belle II analyst is assist the data production group and by validating MC, that is, to ensure that the simulation is consistent with theoretical kinematics derived by hand. We therefore do not need to perform any calculations ourselves to check the validity of the MC we use.

This analysis uses the data generated in the seventh official MC campaign (MC7), originally produced between November 2016 and February 2017. This is conducted within the Belle II Analysis Framework (`BASF2`), a `C++`-based environment equipped with the detector geometry, analysis resources and physics generators, the last of which are `FORTRAN` scripts which incorporate the theoretical phenomenology for the Belle II experiment. Specifically, our MC is generated according to 11.02 GeV COM collisions of e^+e^-, decaying via an $\Upsilon(6S)$ resonance, $\Upsilon(6S) \to [Z_b^+(10610) \to \pi^+ h_b(1P)]\pi^-$. To produce data, the `MadGraph` physics generator calculates the cross sections for $e^+e^- \to h_b(1P)\pi^+\pi^-$ with $\Upsilon(6S)$ beam parameters. The event generator (`EvtGen`), uses supplied decay probability tables and invokes Monte Carlo methods to execute a decay path according to these probabilities.

As discussed in Chapter 1, $h_b(1P)$ has a poorly investigated branching ratio, meaning our decay path requires a topdown, inclusive analysis. The decay tables (Figure 3.1) reflect this by remaining agnostic to

Particle	*Mass*[GeV/c^2]	*Width*[GeV]	*Decay*	*Amplitude*
$\Upsilon(6S)$	11.0190	0.079	$Z_b^{\pm}(10610)\pi^{\mp}$	1.0
$Z_b^{\pm}(10610)$	10.6072	0.184	$h_b(1P)\pi^{\mp}$	1.0
$h_b(1P)$	9.8750	0	$\eta_b(1S)\gamma$	0.492
			ggg	0.508
$\eta_b(1S)$	9.4030	0	gg	1.0

Figure 3.1: Decay table for $\Upsilon(6S) \to [Z_b^+(10610) \to \pi^+ h_b(1P)]\pi^-$, implemented by the data production group to produce signal MC. *Masses used in MC generation are randomly sampled in a distribution centred on the given value and with width given. Amplitudes are arbitrarily assigned.*

possible products, specifying only the number of intermediate gluons. The `Pythia` toolkit can then perform hadronisation, as well as generate further decays. Once the event reaches final state particles, `Geant4` simulates the interaction of these particles with surrounding materials, so as to emulate travel through the subdetectors. For our analysis, we separately look at MC simulated in Phase II and Phase III detector geometry, so as to investigate the difference in measurements at the various stages of SuperKEKB commissioning. `Geant 4` also invokes MC techniques, this time to model random errors in measurements due to detector limitations. This completes the MC data generation.[18].

MC is then stored for analysis as a file consisting of decay particle information, as a series of hits "detected" by each subcomponent. This can be interpreted within `BASF2` to give more useful quantities, such as particle kinematics, likely particle identities, point of origin and flight information. Variables of interest are saved as *.root* files, interpretable by the `C++`-based program `ROOT`. Developed by CERN, the program excels in large data handling and is predominantly used in this analysis to display results derived from MC.

If desired, the generated decay information prior to detector response can also be stored for analysis; this is referred to as *truth MC*. We initially look at truth MC, as it allows us to investigate the physics of Z_b^+ events before incorporating any systematic errors in measurement by the detector. Knowledge of the signatures of an event that does contain Z_b^+ will allow us to identify whether it is present in a random sample of $\Upsilon(6S)$. In this chapter only, we analyse truth MC of both Z_b^+ processes, as well as other e^+e^- processes at a COM energy of 11.02 GeV. From Chapter 4 onwards, we will look strictly at MC with detector response, though truth MC may be implemented as an accuracy check.

3.2 Signal MC

We begin by looking at truth MC generated according to the Z_b^+ process. Our signal to the existence of the Z_b^+ will be the same as suggested in the 2011 and 2016 papers; the invariant mass of the system that recoils from pions in $\Upsilon(6S)$ decays. The definition of the recoil mass is derived from conservation of momentum and energy in decays, demonstrated in Figure 3.2a. Thus, to look for evidence of Z_b^+, we investigate the distribution of recoil masses of pions resulting from $\Upsilon(6S)$ decays. Specifically, we want to restrict ourselves to the pion created alongside the Z_b^+, that is to say, π^- such that $\Upsilon(6S) \to Z_b^+(10610)\pi^-$. We expect that the recoil mass from this partner pion will be consistent with the invariant mass of Z_b^+.

Figures 3.2a and 3.2b demonstrate that not all daughter pions of $\Upsilon(6S)$ will be useful in identifying Z_b^+. The pion associated with Z_b (henceforth referred to as π_1) will have recoil mass equal to the invariant mass of Z_b^+, while the recoil mass derived from the pion associated with $h_b(1P)$ (henceforth referred to as π_2) will not. We will take note of this when analysing the truth MC of our signal process, so that we correctly differentiate between the contribution from π_1 to the recoil mass spectra and that of π_2. We also must consider pions from the hadronic decays of $h_b(1P)$ and $\eta_b(1S)$, as the recoiling system of these pions will also not be the Z_b^+.

The histograms of Figure 3.3 are of the recoil mass and transverse momentum of all pions generated from $\Upsilon(6S)$ decays containing our Z_b^+ process. While our full analysis will occur using Phase II and Phase III MC, we choose to only display histograms of Phase II MC in this case. This is because the physics generation does

$$
\begin{aligned}
P_{e^+} + P_{e^-} &= P_{\Upsilon(6S)} \\
&= P_{Z_b^+} + P_{\pi^-} \\
\implies P_{rec,\pi^-} &= P_{e^+} + P_{e^-} - P_{\pi^-} \\
&= P_{Z_b^+} \\
\implies M_{rec,\pi^-} &= M_{Z_b^+}
\end{aligned}
$$

(a)

$$
\begin{aligned}
P_{e^+} + P_{e^-} &= P_{\Upsilon(6S)} = P_{Z_b^+} + P_{\pi^-} \\
&= [P_{h_b(1P)} + P_{\pi^+}] + P_{\pi^-} \\
\implies P_{rec,\pi^+} &= P_{e^+} + P_{e^-} - P_{\pi^-} - P_{h_b(1P)} \\
&= P_{Z_b^+} - P_{h_b(1P)} \\
&\neq P_{Z_b^+} \\
\implies M_{rec,\pi^+} &\neq M_{Z_b^+}
\end{aligned}
$$

(b)

$$
\begin{aligned}
P_{e^+} + P_{e^-} &= P_{\Upsilon(6S)} = P_{h_b(1P)} + P_{\pi^+} + P_{\pi^-} \\
&= [P_{\pi} + P_X] + P_{\pi^+} + P_{\pi^-} \\
\implies P_{rec,\pi} &= P_{e^+} + P_{e^-} - P_{\pi^-} - P_{\pi^+} - P_X \\
&= P_{Z_b^+} - P_{\pi^+} - P_X \\
&\neq P_{Z_b^+} \\
\implies M_{rec,\pi} &\neq M_{Z_b^+}
\end{aligned}
$$

(c)

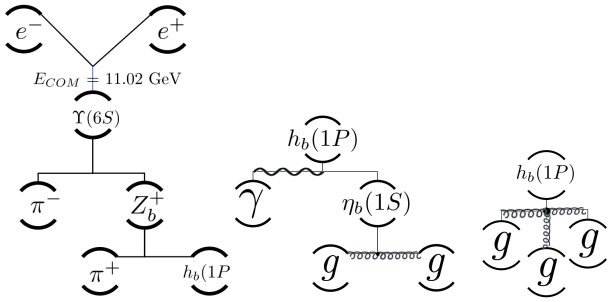

(d)

(e)

(f)

Figure 3.2: Recoil kinematics:
(3.2a) The Z_b^+ four-vector is equal to the four-vector of the system of particles recoiling from it's partnering pion.
(3.2b) Evaluating the recoiling mass from the π partnered with $h_b(1P)$ will not give the Z_b mass.
(3.2c) The recoil mass calculated from these pions will also not give Z_b^+ mass.
(3.2d) The dipion decay featuring Z_b^+ .
(3.2e, 3.2f) $h_b(1P)$ and it's products may decay hadronically, so that $h_b(1P) \to \pi X$, where X indicates any number of other decay products. This emphasises that we need to look at the signature of π associated with Z_b^+ to ensure we obtain the correct mass.

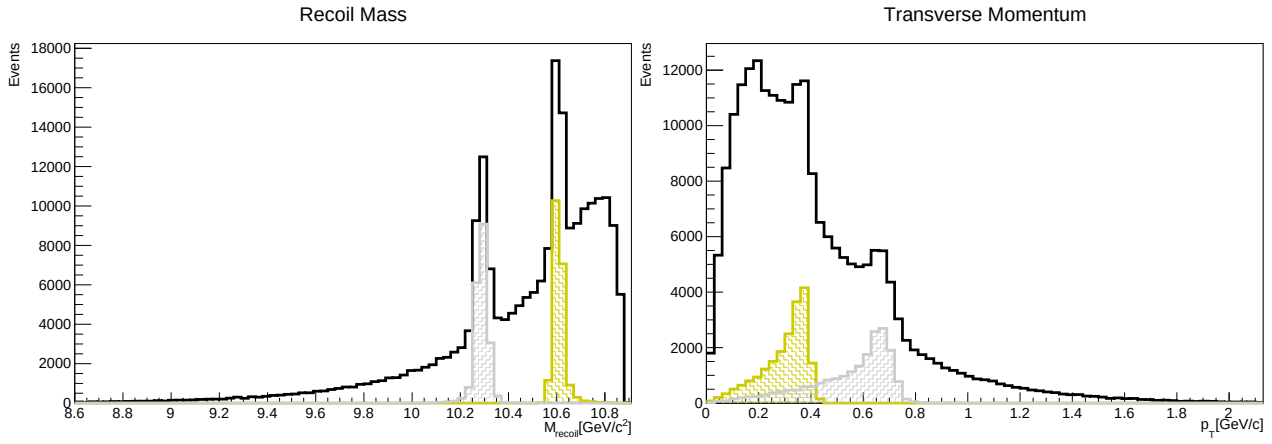

(a) (b)

Figure 3.3: Kinematics of signal pions: Recoil mass and transverse momentum. Black histograms contains all MC true pions from $\Upsilon(6S)$ decay. Gold shaded histograms are MC true pions that have $\Upsilon(6S)$ as their mother particle and are therefore, partnered with Z_b^+. We will refer to these pions as π_1. Silver shaded histograms are MC true pions that Z_b^+ as mother and are therefore partnered with $h_b(1P)$. We will refer to these pions as π_2. We can assume that the large number of pions in the region between the black, silver and gold histograms are from the unspecified $h_b(1P)$ decays.

not vary between phases; the differing geometry only affects detection, as discussed in Chapter 2. Thus as we look at purely generated decay results and disregarding detection, the distributions are identical in both Phase II and Phase III. For completeness, the number of pions generated in both phases are specified in Figure 3.4.

To examine contributions from pions that do not signal the Z_b^+, the histograms are overlayed with the separate distributions of pions the generator identifies as π_1 and π_2. These separate distributions are present as two narrow peaks in Figure 3.3a, coinciding with the peaks of the histogram containing all generated pions. It is very clear that non-π_1 pions hide the contribution of π_1, making it harder to assign significance to the

Detector Phase	*No. of π Generated*	*No. of π with $\Upsilon(6S)$ mother*	*No. of π with Z_b mother*
II	217858	20000	20000
III	217630	20000	20000

Figure 3.4: Table of Generated Pion Statistics: The signal MC contains 20000 $\Upsilon(6S)$ events. When looking for MC event signatures, as simulated in Phase II and Phase III geometry, we restrict the analysis to generated particles rather than detected particles. We see that there is no difference in the number of pions in the dipion decay event, meaning the relatively small difference in the total number of pions generated can be attributed to statistical fluctuation in randomly generated pions from post-$h_b(1P)$ decays.

result. With the π_1 peak in range of $10.61 GeV/c^2$, we see our expectation of the π_1 recoil mass signalling the Z_b^+ is consistent with truth MC. Moreover, we see very little overlap between the peak attributed to π_2, which is centred on 10.295 GeV/c^2. This means that if we analyse pions with only higher recoil mass, we are less likely to include the contribution π_2 without throwing away any π_1 that will contribute to a stronger Z_b^+ signal. We also see that there are 197,858 MC true pions in $\Upsilon(6S)$ decays that are neither π_1 or π_2—almost 10 times more than the number of π_1. The method of demarcating between π_1 and $h_b(1P)$ descendent pions will be discussed in Chapter 4.

We now study the momentum distribution of pions in the event. The histogram of Figure 3.3b, demonstrates more overlap of π_1 and π_2 in transverse momenta than there was for recoil mass. However the peak transverse momenta of π_2 is easily discernible from π_1, occuring at 0.675 GeV/c and at 0.375 GeV/c, respectively. From the momentum 4-vector analysis in Fig 3.2, the relationship between p_T and M_{recoil} can be easily shown, specifically that a lower momentum particle will have a higher recoil mass. This explains the mirroring of peaks between the recoil mass and transverse momentum distributions. The 3-vector momentum magnitude will also be correlated with transverse momentum and therefore recoil mass, explaining the distinct momentum ranges of π_1 and π_2.

The remaining histograms of Figure 3.5 demonstrate the geometry of pions originating from the $\Upsilon(6S)$, specifically the directions in which they are produced, relative to the IP. We clearly see that there is a favoured polar angle, amongst all pions. This is a result of the small boost in $\Upsilon(6S)$, to force it's products towards the forward detectors explained in Chapter 2. Between pions of differing mothers, directly involved in the dipion decay or otherwise, there are no discernible biases in either the azimuthal or polar directions, . This suggests that angle cannot be used to demarcate between π_1 and others, as all distributions are of the same shape: azimuthal symmetry and with slightly more pions emitted down the barrel. This can be further seen in the phase space of the dipion system included in 3.5.

Validation PLOTS

FEYNMAN DIAGRAM

3.3 Background MC

So far, we have focused on signatures present in the recoil mass spectra and the kinematics of our desired process, $e^+e^- \to \Upsilon(6S) \to Z_b^+\pi^-$. We noted that the recoil mass distribution using a random sample of pions from $\Upsilon(6S)$ decays can contain π_2 pions and post-$h_b(1P)$ pions, whose contribution can diminish the significance of a peak at 10.61 GeV/c^2. We also have to consider that other possible decay paths will result from e^+e^- collisions held at COM energy 11.02 GeV, as these may also decay to pions. We now further study signatures in events from the background processes that contribute a significant number pions, as compared to the signatures of Z_b^+.

We will consider two kinds of background; the background due to processes that circumvent the $\Upsilon(6S)$ resonance, referred to as *continuum background* and beam induced background, whose origin was explained in Chapter 2.

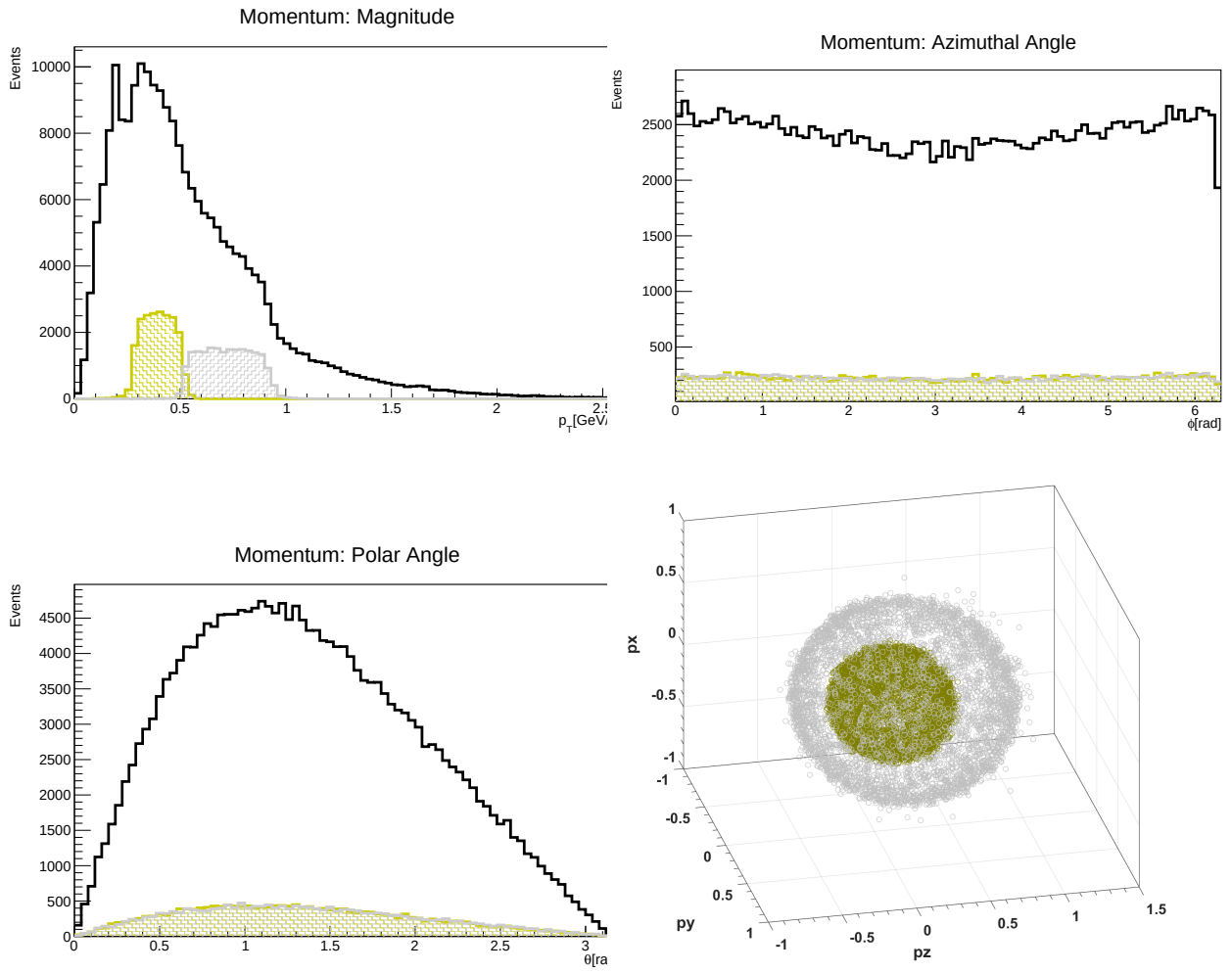

Figure 3.5: Kinematics of signal pions: Momentum 3-vector components and their corresponding phase space. Legend same as in 3.3. Phase space demonstrates that π_1 (gold points) have smaller momentum magnitude than π_2 (silver points), as well as their event shape being more spherical.

3.3.1 Continuum Contribution: $e^+e^- \to q\bar{q}$ and $e^+e^- \to \tau^+\tau^-$

Even though we may expect that 11.02 GeV collisions will favour $\Upsilon(6S)$ production, due to the closeness of the COM energy to it's mass, this is not always the case. Collisions can also result as $e^+e^- \to f\bar{f}$, where f is a quark or charged lepton. In the case of f as a quark, resonant production is restricted to quarkonia of lower mass than $\Upsilon(6S)$, meaning they are created with a boosted momentum to conserve energy. This boosted momentum can result in "jet-like" decay events —this will be implemented in Chapter 4 to decrease the impact of continuum pions on our recoil measurements. These $q\bar{q}$ resonances, where $q \in \{u, d, s, c\}$, can then decay to charged pions via pair production. Continuum background MC is also produced by the Belle II data production group, with the only difference in generation process being the use of the `KKMC` generator instead of `EvtGen` to create $q\bar{q}$ decays.

We also consider the continuum contribution of QED process, $e^+e^- \to \tau^+\tau^-$. The $l \in e, \mu$ cases are not considered, as their masses are too small to decay via pions. Tau pair MC is also generated with the `KKMC` generator, with further τ decays generated with the `tauola` generator. We now study the pion contribution by looking at the truth MC for these background states.

The distributions of pions from continuum events in recoil mass and transverse momentum again show "mirroring". Notably, the unit area normalisation Figure 3.10 demonstrates the shape of the background and signal MC contribution to each variable, so we can best compare their signatures. The background MC contribution follows a smooth, continuous increase in counts with higher recoil mass and lower transverse momentum, much like the post-$h_b(1P)$ pions. The distribution of background recoil mass seems to "peak" at

Continuum Process	*Cross-section*[nb]	*No. of events(II/III)*	*No. of π(II/III)*
$e^+e^- \to u\bar{u}$	1.605	$7.40\times10^7/7.40\times10^7$	9.15×10^7
$e^+e^- \to dd$	0.401	$1.85\times10^7/1.85\times10^7$	$2.31\times10^7/1.15\times10^8$
$e^+e^- \to s\bar{s}$	0.383	$1.77\times10^7/1.92\times10^7$	$4.24\times10^7/4.24\times10^7$
$e^+e^- \to c\bar{c}$	1.329	$6.13\times10^7/6.13\times10^7$	
$e^+e^- \to \tau^+\tau^-$	0.919	$4.24\times10^7/4.24\times10^7$	$1.54\times10^7/7.7\times10^7$

Figure 3.6: The cross-sections of each continuum process at COM energy 11.02 GeV are calculated by the data group. They chose to generate 50 fb^{-1} of continuum events, an arbitrary amount as there is not yet consensus on how long SuperKEKB will operate at $\Upsilon(6S)$ energy.

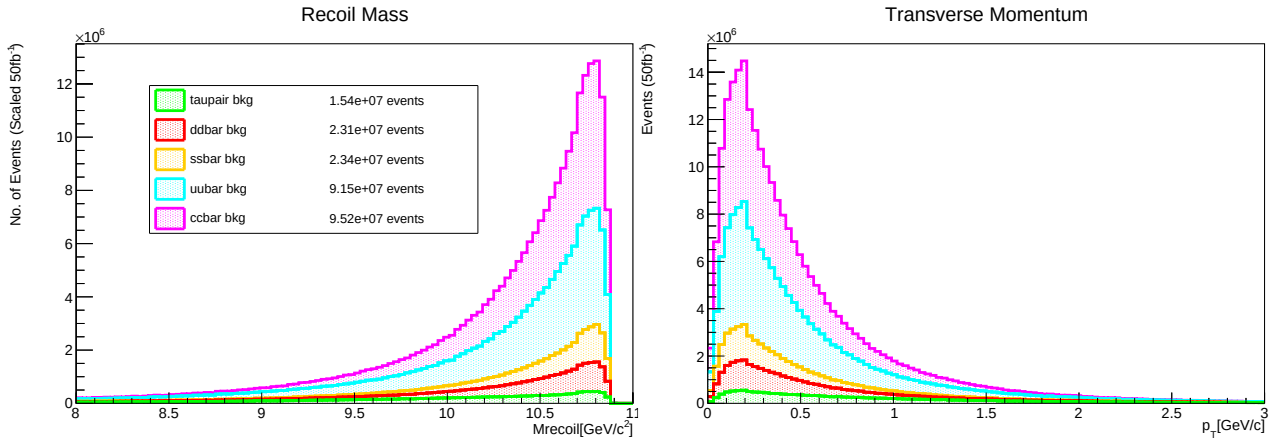

(a) (b)

Figure 3.7: Kinematics of continuum background pions: Recoil mass and transverse momentum.

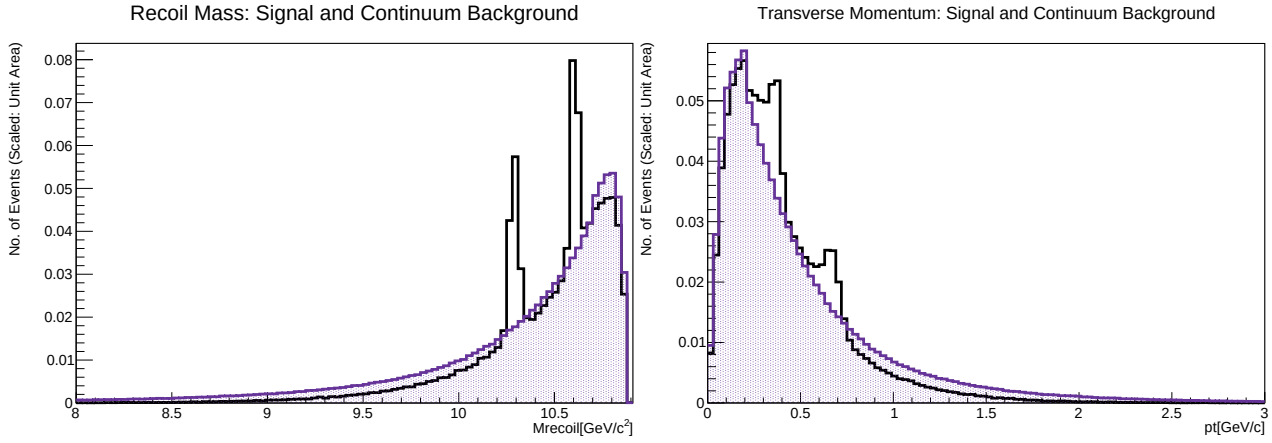

(a) (b)

Figure 3.8: Kinematics of all continuum background pions (purple shaded) and signal MC pions (black): Recoil mass and transverse momentum, where both histograms are normalised to unit area.

10.9 GeV/c^2. This is a result of the number of low momentum pions produced and we must be careful to not confuse this with a meaningful resonance.

The momentum components of the continuum pions show some deviation from signal pions. As expected from the transverse momentum distribution, lower momentum is associated with a larger number of particles. Both background and signal pions demonstrate the same azimuthal symmetry when normalised. The distribution of continuum pion polar angle peaks at a smaller angle than signal pions. This can be explained by the "jet-like" behaviour of higher momentum events vs the more spherical event shape of lower-boosted $\Upsilon(6S)$. Again, this signature will become a key criterion in separating signal pions from continuum ones, beginning in Chapter 4.

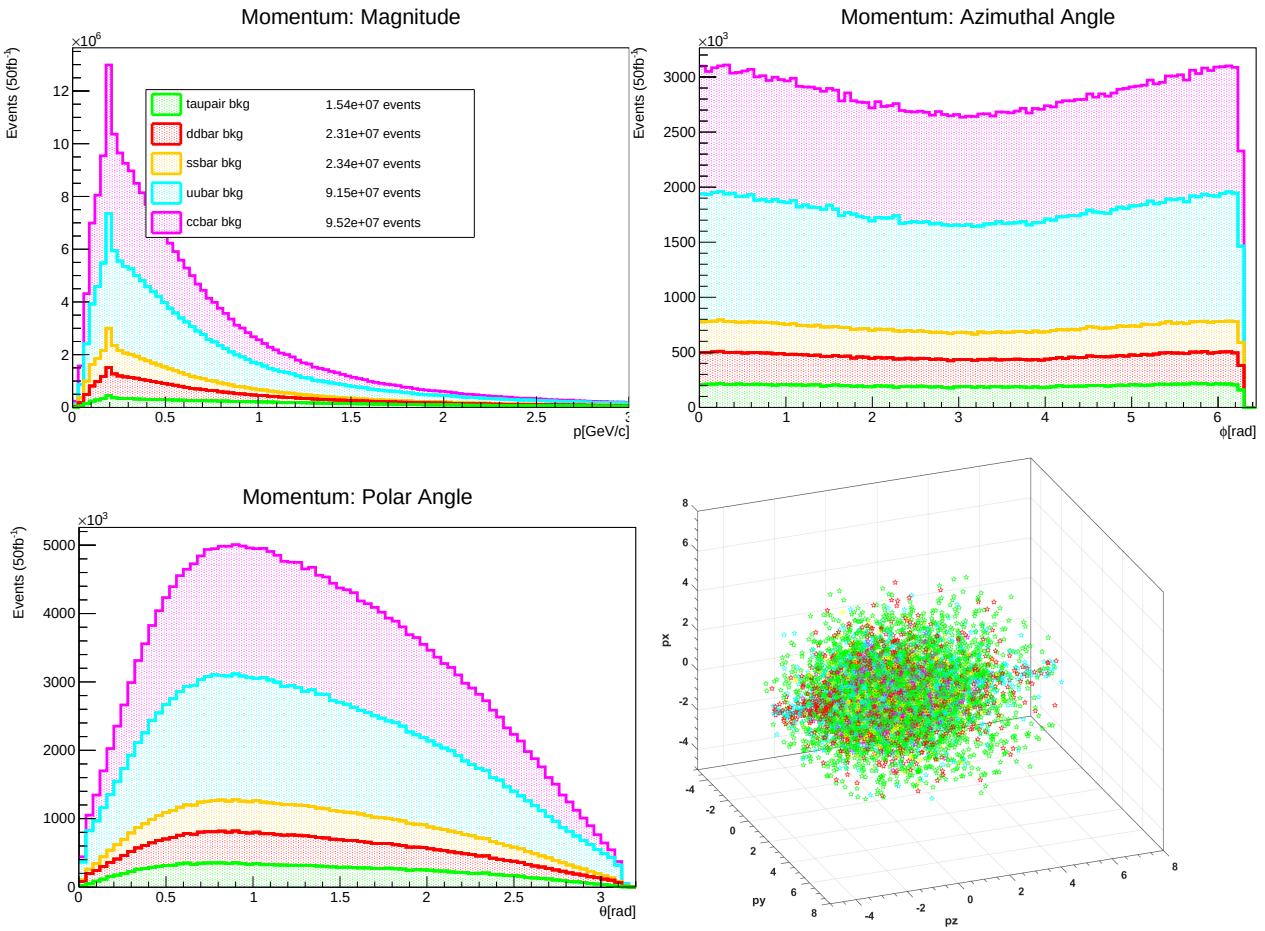

Figure 3.9: Kinematics of continuum background pions: Momentum 3-vector components

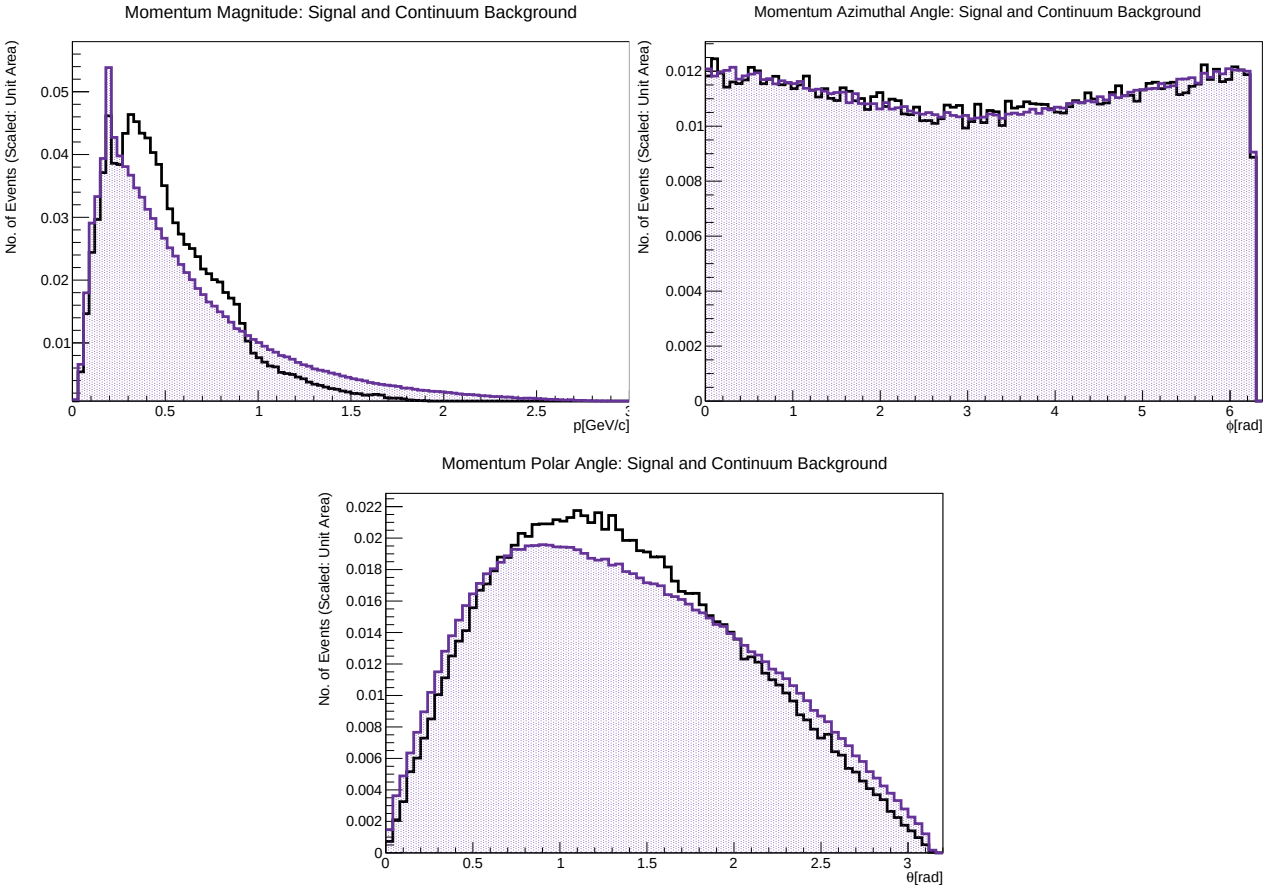

Figure 3.10: Kinematics of continuum background pions: Momentum 3-vector components

3.3.2 Beam Background

The origins of beam background were described in Chapter 2, predominantly due to particle showering from Touschek scattering and beam-gas interactions. To investigate the effect of this on our recoil mass distribution, we will utilise MC that has beam events overlayed with the previous beam-free signal MC. As beam background is an accelerator effect, we look to use MC with detector response for the first time. As the rest of our analysis will take place using beam background, we will look to next chapter to compare and contrast their effect when compared to the truth pion recoil distribution.

Detector Phase	*No. of π Generated*	*No. of π with $\Upsilon(6S)$ mother*	*No. of π with Z_b mother*
II	869162	80000	80000
III	870000	80000	80000

Figure 3.11: Table of Generated Pion Statistics, with Beam Background:

Chapter 4

From Pions to New Particles: Reconstructing and Optimising the Z_b^+ Signal

With knowledge of the pion recoil mass distributions, both signal and background pions, we can now analyse MC with detector response. Due to the limitations of the Belle II hardware we will begin to see the impact of measurement error. Momentum, and thus recoil mass distributions will be more "smeared" than in pure signal MC.

We also saw that the number of pions that could interfere with this distribution, far outweigh those useful in measuring Z_b^+. Without careful thought into what pions we select for our analysis, we may find that a resonance in recoil mass data caused by a Z_b^+ is overshadowed by the contributions of less relevant pions. Therefore, we must maximise our signal to background ratio with effective selection criteria. Our analysis proceeds as a standard experimental particle physics "bump search"; we would like to investigate how to best use selection criteria to separate background pions from our measurements without losing signal pions, so that we may best see our "bump" in real detected events.

4.1 Preselection and Reconstruction

We use `BASF2` to interpret both our signal and background MC. In a more typical, exclusive reconstruction, we are able to rebuild candidates entirely from their detected daughter particles. As mentioned earlier, the branching ratios of $h_b(1P)$ are not well known, so reconstruction of $h_b(1P)$ and thus Z_b^+ will not proceed in this way. Instead, we consider a list of all possible combinations of final state pions pairings of opposing charge, as is dictated by our signal decay path. These pairs are then reconstructed, yielding a state A, that is the sum of π^+ and π^- four-vectors, such that $A \to \pi^+\pi^-$. This is not a real particle, but a useful construction to examine the number of possible pion pairings. Evaluating the mass of the system that recoils against state A (the scalar invariant of the four vector $P_{rec,A} = P_{e^-} + P_{e^-} - P_A$) will be the same as that of $\pi^+\pi^-$, allowing us to use this as a constraint on pions in this list. Applying this constraint limits the pions that contribute to the final individual recoil mass distribution, so that they are more like to be those in $\Upsilon(6S) \to h_b(1P)\pi^+\pi^-$ and thus, $Z_b^+ \to \pi^+ h_b(1P)$. This decay requirement placed on pions at reconstruction level is referred to as *preselection* criteria, as it ensures we begin with the correct final state pions and minimize the number of candidates per event. We consider pairings consistent with $h_b(1P)$ if 9.8 GeV/c^2 $< M_{rec,\pi^+\pi^-} <$10 GeV/c^2, as implemented by the 2016 Belle analysis.

$$
\begin{aligned}
P_{e^+} + P_{e^-} &= P_{\Upsilon(6S)} = P_{Z_b^+} + P_{\pi^-} \\
&= P_{h_b(1P)} + P_{\pi^+} + P_{\pi^-} \\
\implies P_{rec,\pi^-\pi^+} &= P_{e^+} + P_{e^-} - P_{\pi^-} - P_{\pi^+} \\
&= P_{h_b(1P)} \\
\implies M_{rec,\pi^-\pi^+} &= M_{h_b(1P)}
\end{aligned}
$$

(a) Preselection criteria justification

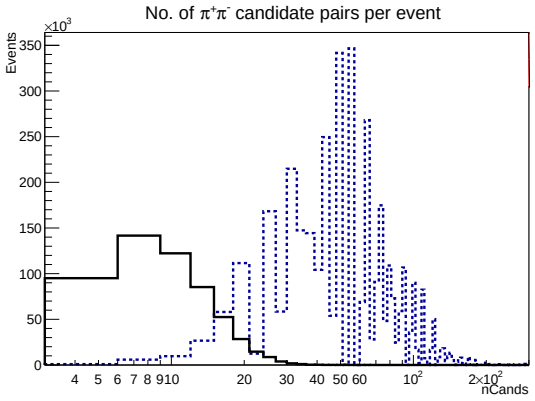

(b) The combinatoric background is cut out drastically with preselection criteria.

Figure 4.1: The equation (a) demonstrates that the mass of the system recoiling against two pions is that mass of $h_b(1P)$. Histogram (b) demonstrates how the number of candidate dipion pairings reduces drastically before (blue dotted histogram) and after the preselection criterion is applied (black histogram).

This preselection criterion is used to combat the main disadvantage to an inclusive reconstruction: *combinatoric* background. That is to say, if a particular Z_b^+ process produces post-$h_b(1P)$ pions, we can unintentionally introduce double counting. For example, we may add the pions π_1 and π_2 to our list to analyse as they satisfy the criterion as a pairing, but also add the pairings $\pi_1\pi_{h_b(1P)}$ and $\pi_2\pi_{h_b(1P)}$. We attempt to limit the combinatoric background by placing further preselection criteria on pions admitted to the pion list: that the mass of the system recoiling against the pion pair is within error of the $h_b(1P)$ mass. The justification of this is demonstrated in 4.1a. This does not completely rid us of post-$h_b(1P)$ pions, but still limits the number of candidate pairings per event. It is not impossible for a pion to have three-momentum within the range of π_1 or π_2 (see Figure 3.5).

4.2 Selection Criteria

4.2.1 Studying the Belle Criteria

After applying preselection criteria and reconstructing the $\pi^+\pi^-$ pairs, we can consider selection criteria. Such criteria are imposed to maximise the signal to background ratio. For example, we saw in Figure 3.3b that a large number of π_2 had transverse momenta of 0.5 GeV/c or greater. If we were to consider the recoil mass of pions with transverse momentum less than 0.5 GeV/c, we could expect a smaller contribution from π_2 without susbstantial losses in the number of π_1.

The selection criteria of the Belle 2016 paper will be a launch pad for this analysis. We expect better performance when applied to Belle II events over Belle events, due to enhanced tracking efficiencies. We will measure the efficiency of such selections, and look into the distribution of our selection criteria in signal and background MC for Phase II and Phase III geometry with beam background.

In Figures 4.4 and 4.7, we see two very small peaks occuring around 10.3 GeV/c^2 and 10.6 GeV/c^2 in the single pion recoil mass calculated for both Phases II and III. These are consistent with the peaks we saw in truth-matched MC, which can be attributed to π_2 and π_1 respectively. The overall shape of the distributions are different to the truth MC —we can attribute this to the preselection cut that limited the recoil mass of pion pairs, and thus of individual pions. The recoil mass distribution for Phase III differs from that in Phase II as it admits a smaller peak in signal MC at 10.9 GeV/c^2. We saw the correlation between low momentum pions resulting in high recoil mass in Chapter 3, so we know there is a surplus of low-momentum pions detected in Phase III. This is to be expected, as the lack of VXD subdetectors in Phase II means that such low-momentum particles cannot be seen. This is demonstrated by the loss in tracking efficiency in this region. We can also

	To exclude pions produced in beam background.	
Variable	*Definition*	*Criterion*
dz	Point of detection: z component displacement with respect to the interaction point. Sets maximum tolerated distance for particles to be considered as originating from the IP. Beam background particles are not created at interaction point.	dz<2cm
dr	Point of detection: radial displacement with respect to the interaction point. Sets maximum tolerated distance for particles to be considered as originating from the IP. Beam background particles are not created at interaction point.	dr<0.3cm

Figure 4.2: Selection Criteria Implemented in 2016 Belle Analysis.

	To exclude particles misidentified as pions.	
Variable	*Definition*	*Criterion*
piPIDe	Pion particle ID: The probability that a tagged pion is an electron.	PIDe<0.9
piDLLK	Delta Log Likelihood: Ratio of π over K likelihoods, derived from subdetectors	DLLK>log(0.1)
piDLLP	Delta Log Likelihood: Ratio of π over K likelihoods, derived from subdetectors	DLLP>log(0.1)
	To exclude pions produced in continuum events.	
Variable	*Definition*	*Criterion*
R2	Reduced Fox Wolfram Moment: Ratio of "jet-like" event behaviour to "spherical", low momentum events	R2>0.3

Figure 4.3: Selection Criteria Implemented in 2016 Belle Analysis continued.

attribute this to beam background as we did not see this in the Phase III background-free signal MC. Once the quality cuts are applied to our distribution, we expect a distribution like that in the background-free case.

The histograms in Figures 4.4 and 4.7 expresses the fraction of signal events to background events per bin in the recoil mass distribution. This is examined so as to get an idea of how well our critera separates signal and background. For the peak at 10.6 GeV/c^2, the ratio of signal events to background events is approximately 1.35% and 1.24% in Phase II and Phase III, respectively. Thus, without applying any selection criteria, identifying the resonance is unlikely; extrapolating from this percentage, for every pion that we tag as signal to the existence of Z_b^+, there will be 70 or more originating from non-$\Upsilon(6S)$ decays.

The separating power of R2 in signal-continuum background discrimination can seen in Figures 4.5a and 4.8a. With log event scale, it is simple to see that the number pions created in $\tau^+\tau^-$ events peak in a region of the R2 distribution where there are almost no signal pions. This is a result of $\tau^+\tau^-$ events created at higher momentum, restricting the event shape to be jet-like, rather than unbiased, spherically symmetric event shape of lower momentum events, like our signal. The peak of the R2 distribution in tau pairs varies from the quark-based continuum, as it is a QED process. While the criterion employed by Belle, R2 <0.3, omits a number of signal events, we will see later in this chapter that these events were sacrificed for lower background contributions. We will also attempt to see if we can optimize this criteria, by changing the upper bound of R2 values selected. The overlayed gold region indicates the range of R2 values assumed by pions that originate

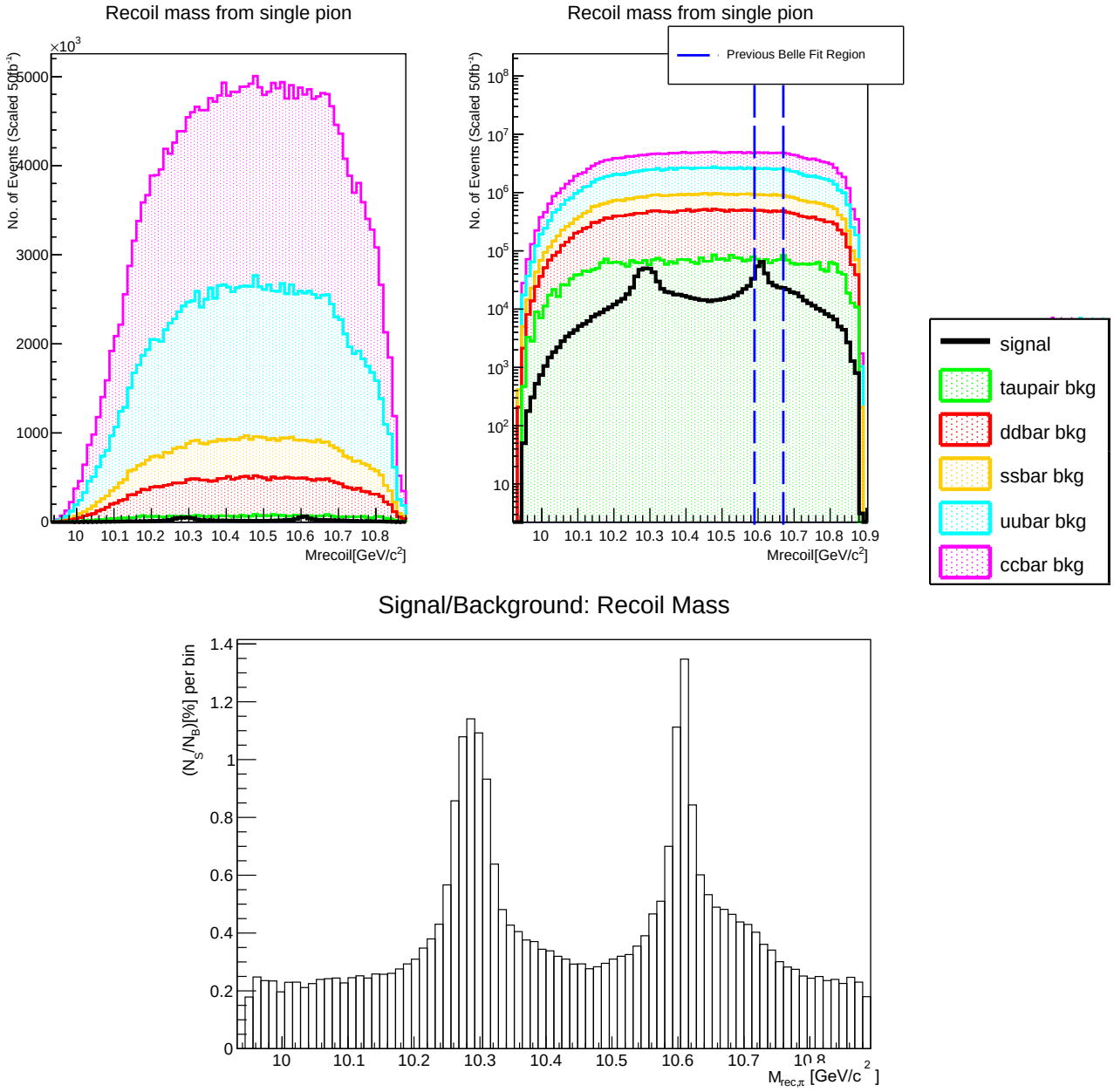

Figure 4.4: Phase II: Recoil mass without *(top left)* and with logarithmic event scale *(top right)*, legend with number of pions detected *(middle)*, signal-to-background ratio plot *(bottom)*. The signal and continuum process colours remain constant throughout this analysis, where continuum contributions are stacked and signal contribution is overlayed.

from pairs that give recoil mass $h_b(1P)$ and also have singular recoil mass within tolerance of Z_b^+ mass used by Belle, 10.59 GeV/c^2 $<M_{rec,\pi}$ $<$10.67 GeV/c^2.

The variables that allow us to distinguish between pions resulting from e^+e^- collisions, and those that originate from stray beam electrons interacting with matter are dz and dr. Figures 4.5b, 4.8b, show that the z-displacement from the interaction point to point of detection is not useful in distringuishing continuum and signal events. We note that as continuum events occur as $e^+e^- \to q\bar{q}$ and $e^+e^- \to \tau^+\tau^-$, continuum pions will be created at the interaction point just as signal would. The dz distribution demonstrates that considering subsets of smaller dz omits as much signal as it does continuum in both phases, meaning it is not favourable to cut on this. This same trend is demonstrated in the dr distributions Figures 4.5c and 4.8c, so we will use the same Belle cut in our analysis. We should see that once the cut is performed, the peaks of recoil mass in Phase III are softened, as we remove detected far from the point of interaction.

The final three variables to consider are those related to particle identification. Their distributions in Phase II and Phase III demonstrate their performance. We see in Figures 4.6b, 4.6c and their Phase III counterparts that the number of correctly identified pions increases with DLLK and DLLP, similarly that in Figure 4.6a that

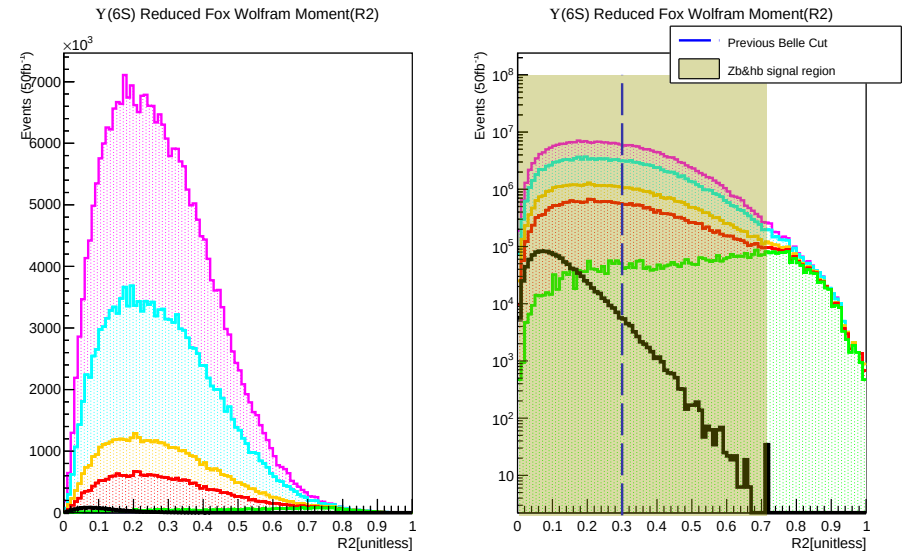

(a)

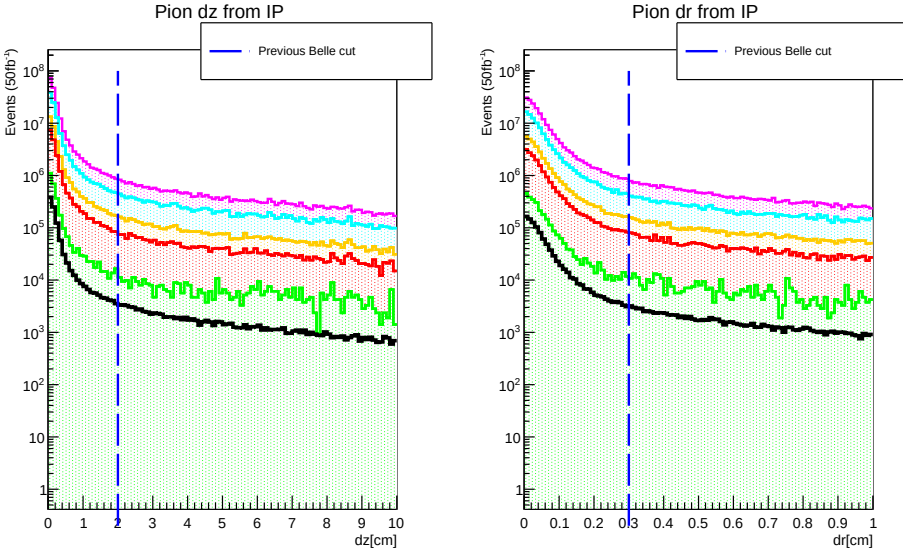

(b) (c)

Figure 4.5: Phase II: Selection Criteria, R2, dr and dz distributions. Distributions of dr and dz without logarithmic scale are omitted for clarity. Legend and number of pions are same as in Figure 4.4.

the number of true pions increases with a lesser electron identification probability. Again, we see that these variables do not discriminate between continuum and signal; considering subsets of pions with higher likelihood to be a pion over a kaon or pion over a proton, or with lower electron identity probability does not vary the amount of continuum events admitted. Again, for this reason we will not restrict our subset any further than what was implemented at Belle based on these values. We should find that the increased vertexing capability of the Belle II detector allows for better identified pions even with the same cuts, than with that of the original Belle detector.

We now examine the distributions after the quality cuts(Figures 4.11,4.12,4.13,4.14) specifically examining the effect with and without R2. We will consider the resultant power of each cut on recoil mass distribution in a signal-to-background plot. For Phase II, we see the signal to background ratio increase to 2% after quality cuts and 3.4% after including the quality and R2 cuts. Phase III similarly increases to 1.81% and to 2.9%. The impact of the selection criteria is especially evident in Phase III distributions, as we see the higher recoil mass beam background contribution diminish as predicted. Reflecting on the performance of the original Belle criteria between the phases seems to be near-identical, suggesting that this analysis can be efficiently run in Phase II and Phase III.

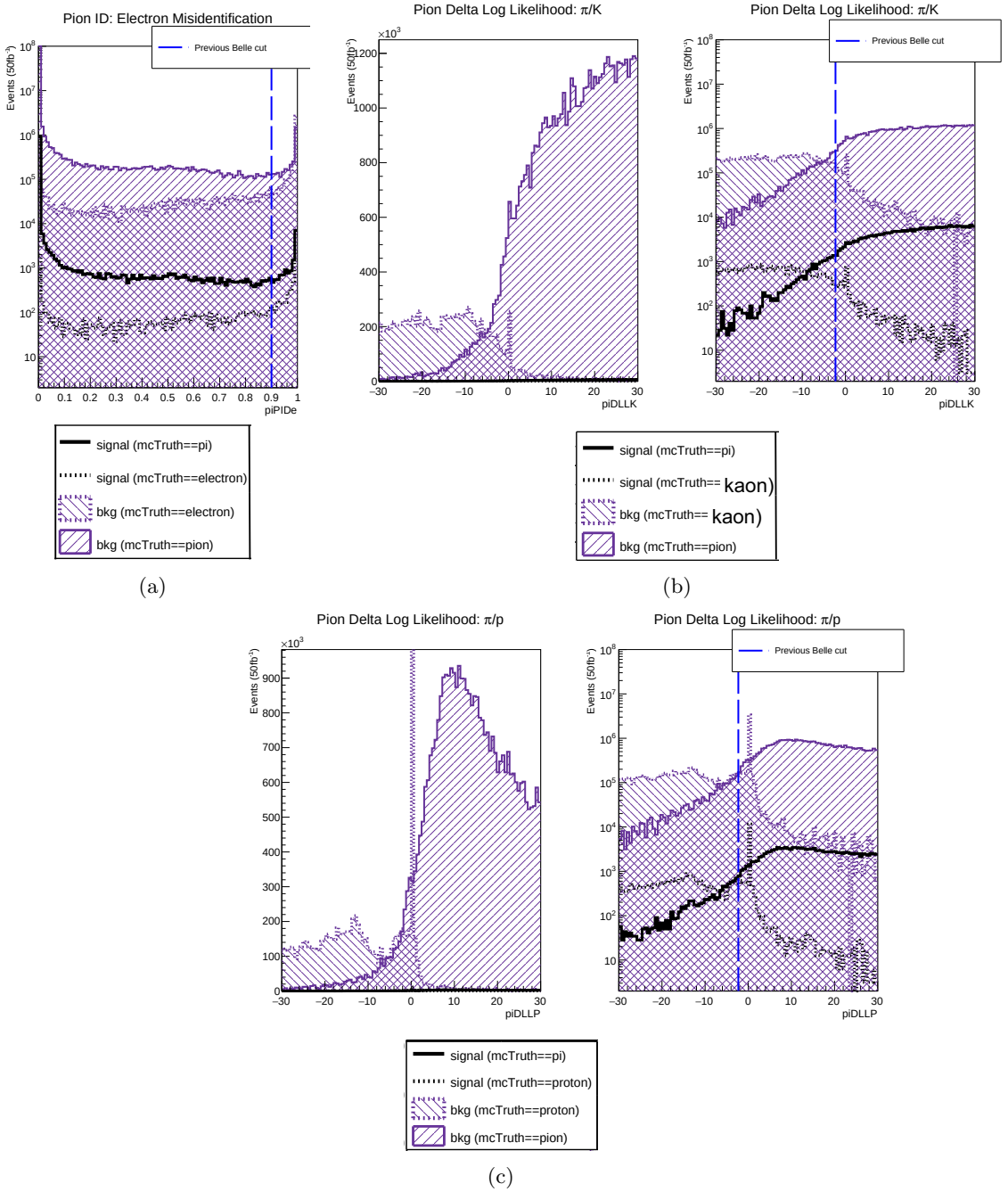

Figure 4.6: Phase II: PID Selection Criteria. Distribution of piPIDe without logarithmic scale is omitted for clarity.

4.2.2 Optimising the Belle Criteria: R2

Even after applying the Belle cut to minimise the contribution from continuum pions, R2 <0.3, we still see a large amount of background processes that conceal our measurements of the Z_b^+ resonance in single pion recoil data. We can analyse if the selection of pions according to $R2<0.3$ is the most efficient cut on the Reduced Fox Wolfram Moment, or if a different value can saves more pions, whilst removing more irrelevant pions. This is done by considering the *integrated significance*. The significance of a peak can be quantified as as $\Sigma = \frac{N_S}{\sqrt{N_S+N_B}}$, where N_s and N_b are the number of signal and background event in the vicinity of the peak. This quantity is derived from treating our measurements as a stochastic process (true, as we have invoked MC techniques), which implies that our measurements are Poisson distributed. With the total number of counts being $N_S + N_B$, we can estimate the standard deviation to be $\sigma = \sqrt{N_S + N_B}$, from the Poisson distribution assumption. Thus, to measure if the number of signal events are consistent with background, we can divide the number of signal events by σ, to see how many standard deviations the number of signal events are from the mean. This gives us an indication of how probably the number of signal events are a random fluke within background, or a true anomalous process.

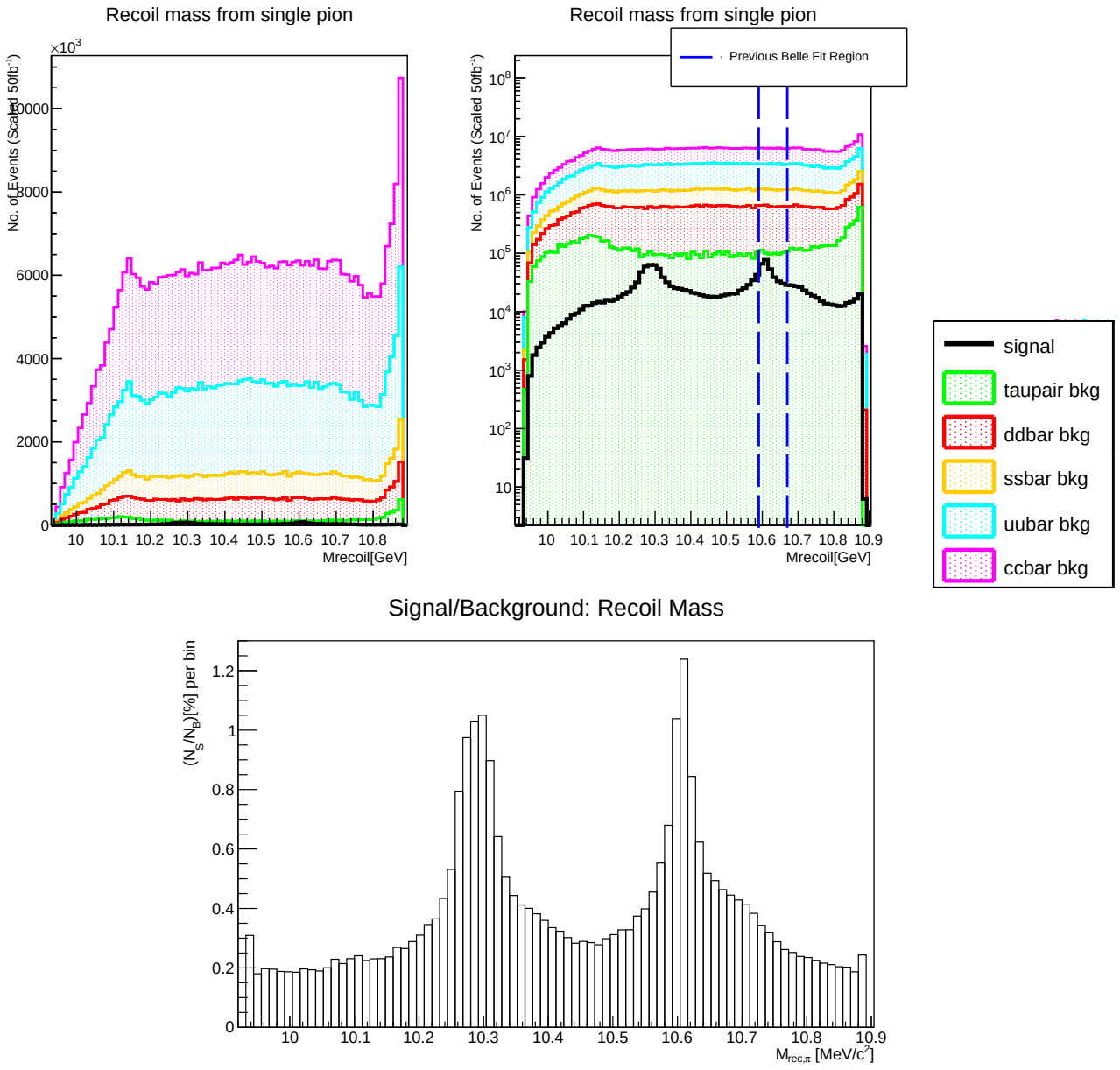

Figure 4.7: Phase III: Recoil mass without *(top left)* and with logarithmic event scale *(top right)*, legend with number of pions detected *(middle)*, signal-to-background ratio plot *(bottom)*

In this case, we want to choose to cut on some R2 value, r <1, such that the subset of events with R2 between $[0, r]$ has the largest significance. In this way, we can perform the best cut on the recoil mass distribution to eliminate background and retain signal pions. We produce a figure of merit plot, that demonstrates how Σ changes depending on our choice of R2 cut.

Figure 4.15 demonstrates that R2 <0.3 is not the most efficient cut. We perform the suggested cut, R2 <0.135, with the results demonstrated in Figure 4.16 and Figure 4.17. With signal to background ratio of 7.1% in Phase II and 5.8% in Phase III, we see large improvement with this new cut over the one used in Belle. Despite having already demonstrated an improvement in selection criteria performance implemented in Belle II MC, we can further attempt to improve continuum suppression. Within the `BASF2` software, we have access to 32 variables associated with continuum suppression, of which R2 is one. We will not, however, test all 32 variables to cut upon; we look to a machine learning and multivariate analysis package for `ROOT` in the next section, to create a signal-background classifying variable from the contrinuum suppression variables for us.

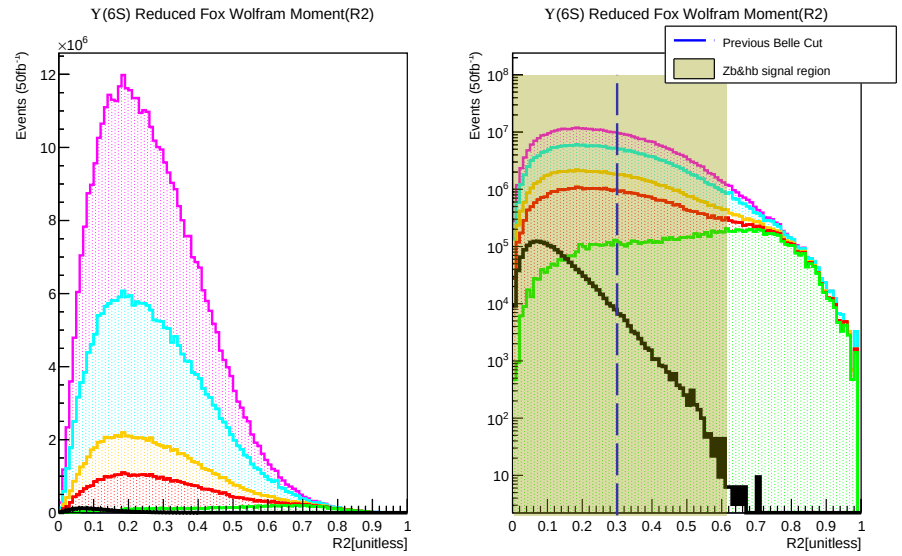

(a)

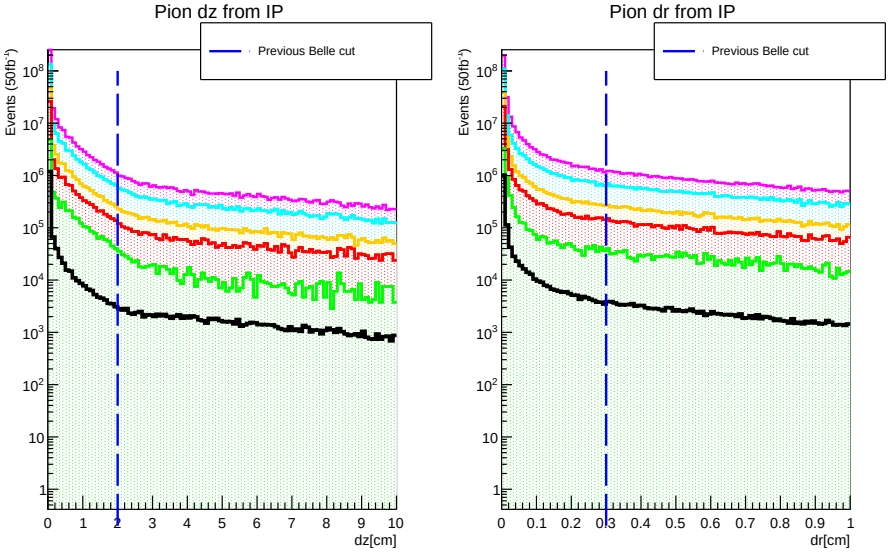

(b) (c)

Figure 4.8: Phase III: Selection Criteria, R2, dr and dz distributions. Distributions of dr and dz without logarithmic scale are omitted for clarity. Legend and number of pions are same as in Figure 4.4.

4.3 Multivariate Analysis with TMVA

The *Toolkit for Multivariate Data Analysis with ROOT*, or TMVA, is a set of software tools integrated into ROOT that can be used in analyses where a number of variables can describe a scenario, in our case, the 32 variables that have varying separating power of signal and continuum events. TMVA methods involve providing a sample of known background events, known signal event and the set of variables that may have unique distributions over signal and background. From this, the program explores which combination of variables create the most distinct distributions between signal and background, outputting this variable (the *classifier*) to the user. The toolkit can also be used to test the classifier on separate sample of data, to measure how well it performs in classifying an event as either signal or background.

For our analysis, we use the *boosted decision tree*(BDT) multivariate classification method. It is relatively simple when compared to the other methods, especially as we already have the complexity of 32 variables. The specifics of the classification method can be found in the *TMVA Users Guide*[19], but a brief summary is provided here. It is named thusly as it's method can be represented by a tree diagram, with each level producing two branches from the "decision" to cut on a data set —one branch consistent with the cut and the second branch it's complement. In our case, we input a sample of signal and background MC and the toolkit registers

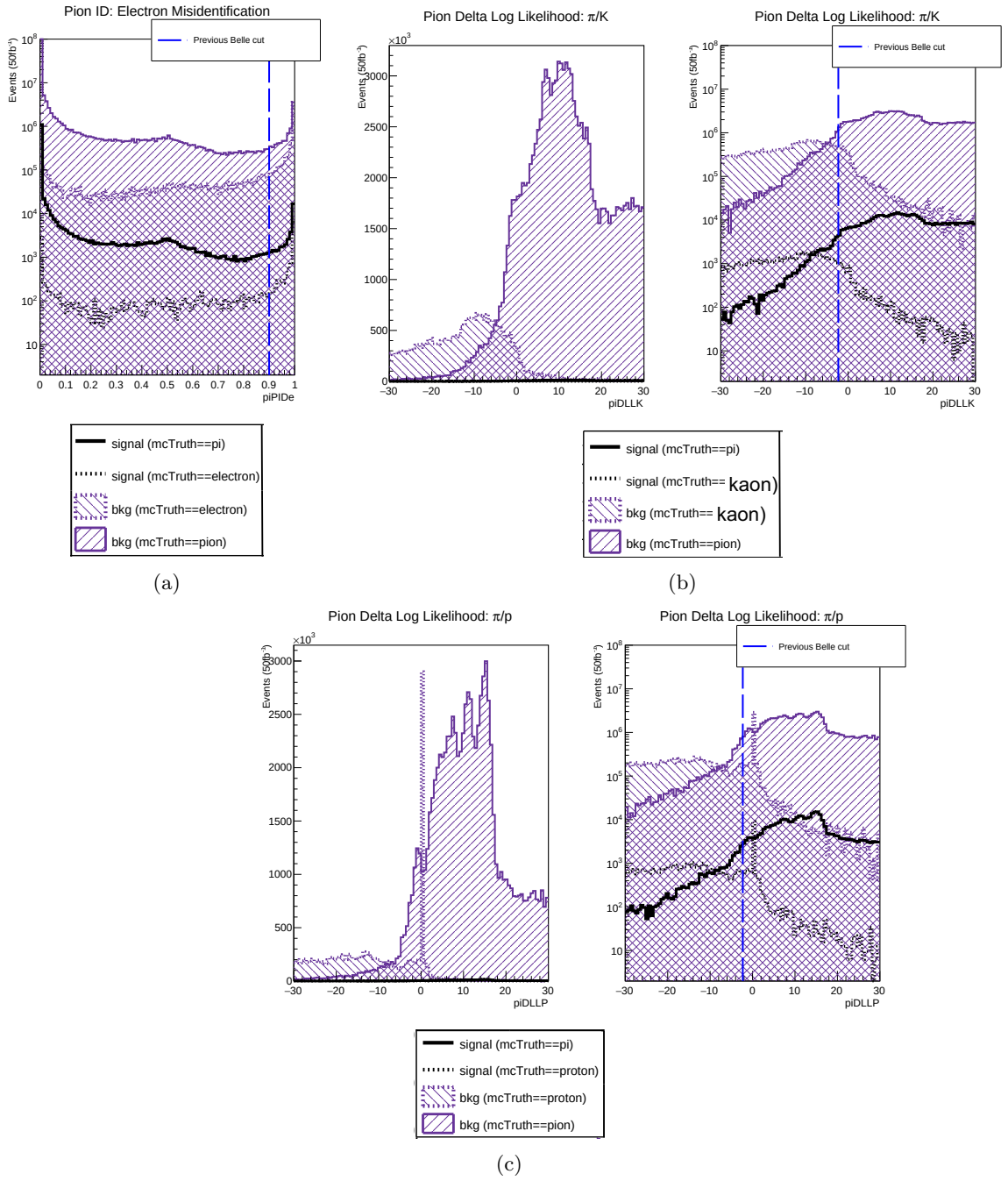

Figure 4.9: Phase III: PID Selection Criteria. Distribution of piPIDe without logarithmic scale is omitted for clarity.

the origin of each event, before mixing them together. The toolkit then "grows" a decision tree by making a series of cuts on various continuum suppression variables, attempting to split the mixed sample into background and signal. The "boost" occurs when the number of background and signal events for a tree are tallyed, where each decision sequence is assigned a weighting. Those sequences that perform worse receive a higher weighting, meaning the method will avoid performing cuts of higher weighting. The method repeats until the data is separated into signal and background and returns a classifier variable based on the successful decision sequence, normalised so that a value of -1 indicates an event is background-like and 1 is signal-like.

Once the classifier is trained, it can be implemented in new data. Due to the lack of enough $\Upsilon(6S)$ samples, we divide our sample in half, with half to train the classifier and half to test the classifier. The files were divided according to the order the events were detected, with odd numbered events becoming training samples and even numbered events becoming testing samples. Due to the MC method of generation, the outcome of each event is independent of the one before it, meaning we have introduced no biases by using events from the same sample file.

Ultimately, we do not use all 32 continuum variables. This is because we want to avoid using any continuum

Phase	*Process*	*Event weighting*	*No. of pions*
II	$e^+e^- \to u\bar{u}$	831.7129916	1.27×10^6
II	$e^+e^- \to d\bar{d}$	208.049842	9.27×10^7
II	$e^+e^- \to s\bar{s}$	207.9417293	2.33×10^7
II	$e^+e^- \to \tau^+\tau^-$	471.1111111	4.20×10^6
II	$e^+e^- \to c\bar{c}$	696.3218756	1.27×10^8
II	$e^+e^- \to [Z_b^+ \to h_b(1P)\pi^+]\pi^-$	3.125	1.25×10^6
III	$e^+e^- \to u\bar{u}$	831.9748159	1.48×10^8
III	$e^+e^- \to d\bar{d}$	207.8931991	3.69×10^7
III	$e^+e^- \to s\bar{s}$	225.7750003	4.11×10^7
III	$e^+e^- \to \tau^+\tau^-$	471	1.01×10^7
III	$e^+e^- \to c\bar{c}$	695.5209314	2.02×10^8
III	$e^+e^- \to [Z_b^+ \to h_b(1P)\pi^+]\pi^-$	3.125	1.79×10^6

Figure 4.10: Numerical summary of event, the number of pions contributed from each process: It is important to note that due to computational constraints, running over all 50 fb^{-1} of MC events were not feasible. Instead, the number of events in one sample, n_{sample}, were scaled by factor k so as to obtain the number of events in 50 fb^{-1}. This was performed as $n_{50fb^{-1}} = k \times n_{sample}$. For the signal MC, 80000 events were generated. To evaluate the number of events here, we applied $n_{50fb^{-1}} = \mathcal{L}\sigma$, where σ is the cross-section of signal event measured in the 2016 Belle analysis. We took σ=2.5 pb from the Born cross section fit in Figure 1.14b. From this, the signal event weighting could be derived.

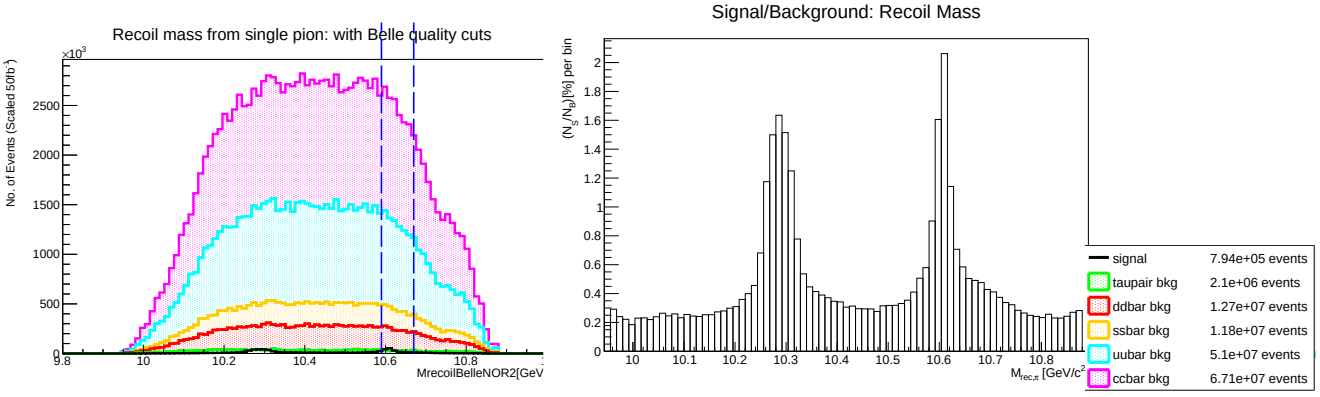

Figure 4.11: Phase II, after Belle cuts

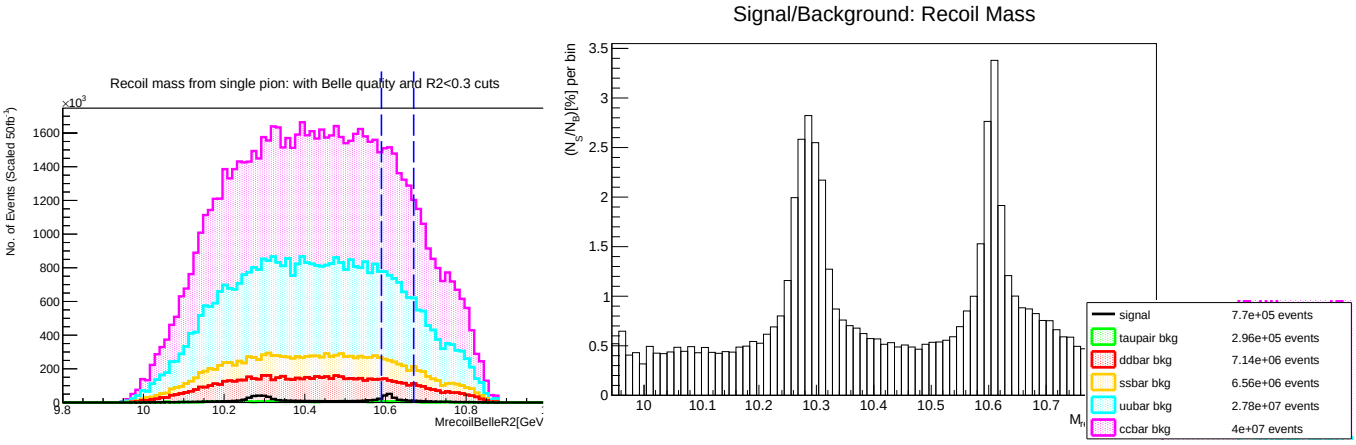

Figure 4.12: Phase II, after all Belle cuts.

suppression variables that are linearly correlated with our recoil variable. Cutting on these may artificially shape the background distribution to the shape of the signal, giving false significance to peak. To ensure this was not the case, we examined 2D histograms of single pion recoil mass versus each continuum suppression variable, looking to exclude those that exhibited linear correlation. Those that remain are listed, with their individual separating power, in Figure 4.20.

Figure 4.18 and Figure 4.19 demonstrate the distribution of the classifier. The signal contribution peaks in the positive values, while $q\bar{q}$ contribution peaks at -0.1 and taupair contribution peaks at -0.3. This is consistent

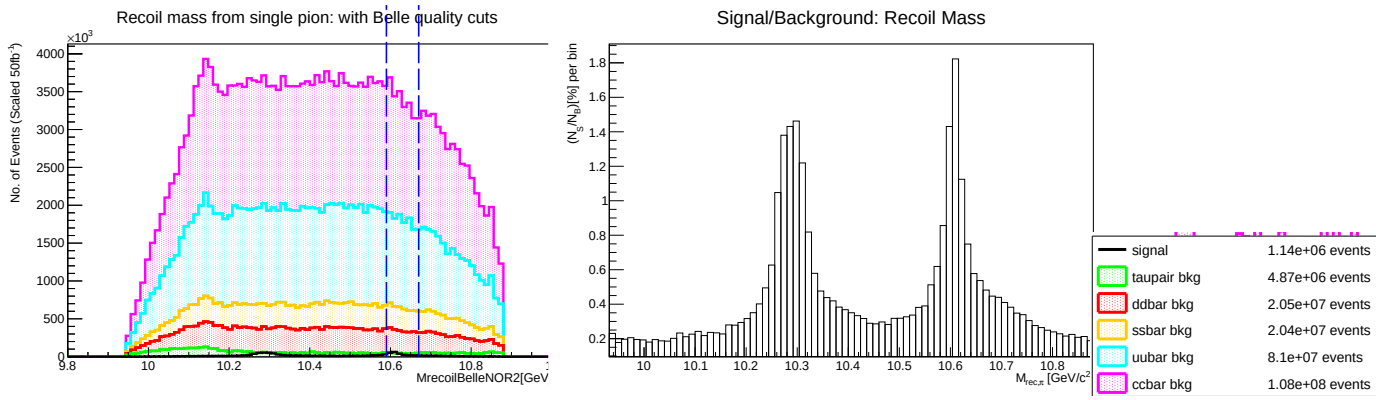

Figure 4.13: Phase III, after Belle quality cuts

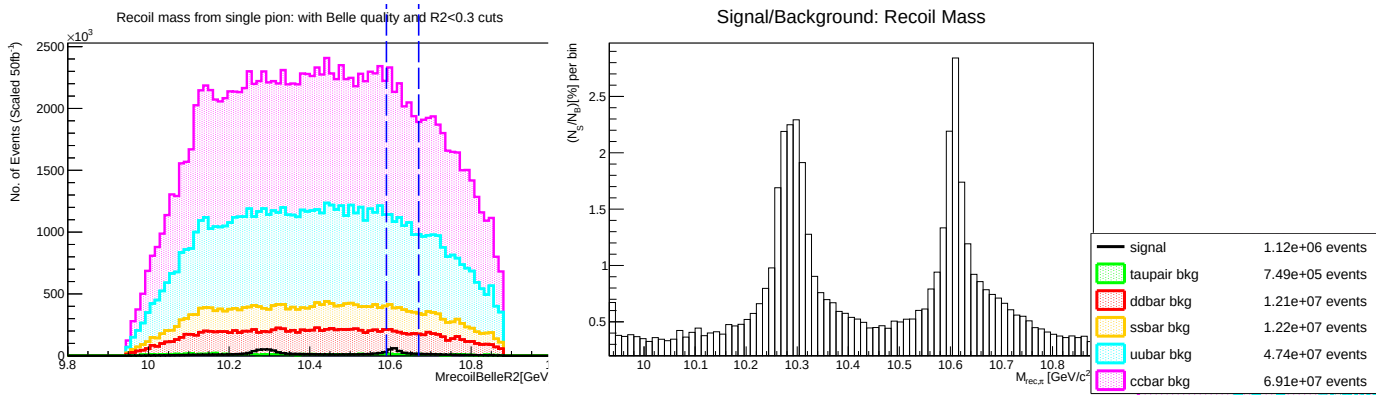

Figure 4.14: Phase III, after all Belle cuts.

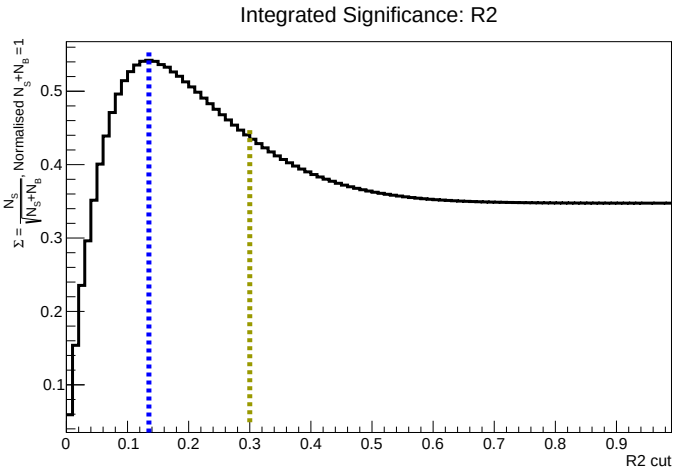

Figure 4.15: Figure of Merit Phase II: The integrated significance is evaluated for subsets of pions with R2 between 0 and r, where r values are R2 cut values, here on the x axis. The gold line indicates the integrated significance of the original R2 <0.3 cut, with $\Sigma = 0.44$. The blue dotted line corresponds to the cut R2<0.135, which gives the maximum $\Sigma = 0.54$. The integrated significance plot for Phase III is consistent with this, admitting the same cut R2 <0.135 .

with negative values associated with background and positive values associated with signal. If we find that a cut such that BDT >0 maximises integrated significance, we can be sure our classifier has been trained correctly. We proceed to constructing a BDT figure of merit, in the same way we did for optimising the R2 cut. The optimal cut is demonstrated in Figure 4.21. The result of this cut in Phase II and Phase III is demonstrated in Figures 4.22 and 4.23.

R2 is listed as the most powerful separating variable in Figure 4.20. Nevertheless, according to the signal to background ratio in the recoil mass distribution after cutting on the classifier output, implementing many continuum suppression variables in TMVA has more separation power in the 10.61 GeV/c^2 region that using R2 alone. The ratio is as high as 14% in Phase II and 10.2% in Phase III, tau pair contribution has been completely eradicated in this Phase. It is important to note that with further cuts, from least effective R2 <0.3 to most

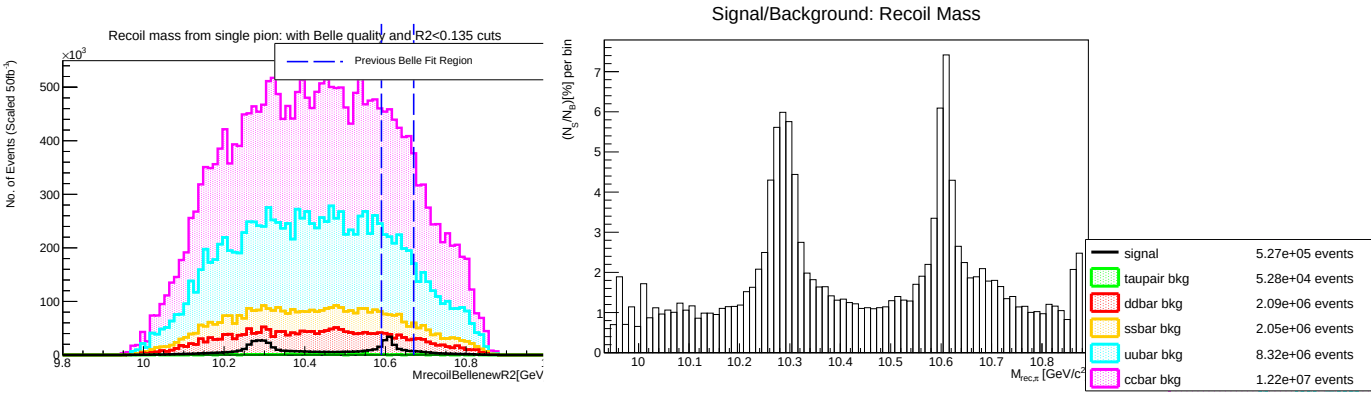

Figure 4.16: Phase II, after quality cuts and R2 <0.135 .

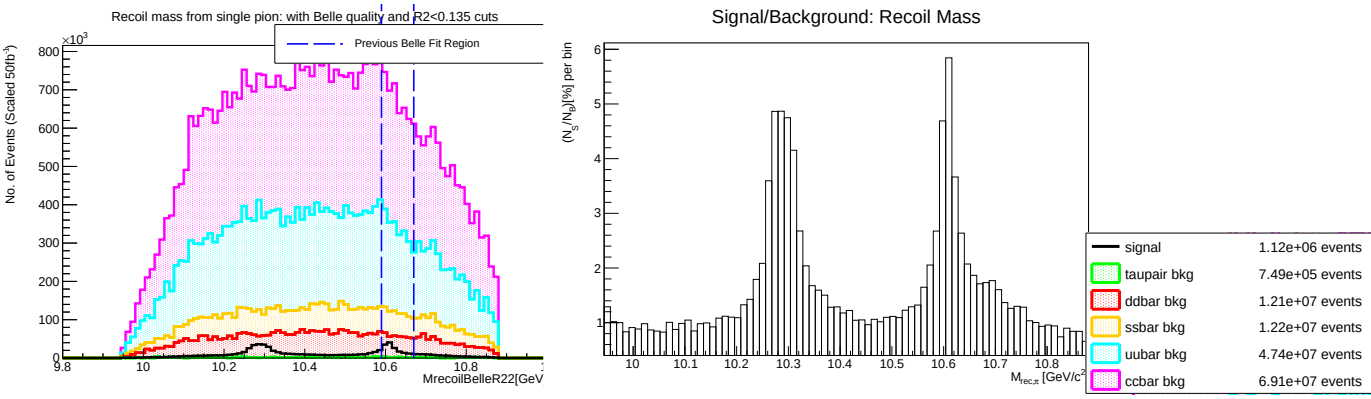

Figure 4.17: Phase III, after quality cuts and R2 <0.135 .

effective BDT <0.0669, we see futher deviations from a smoothly changing number of events per bin. Recall our need to weight the data, as described in 4.10. When the weight of each event becomes non-negligible compared to the scale of events, more fluctuations can be seen. This reduction in statistics should be clarified in further studies, as fluctuation in data points will affect the fit quality we will perform in Chapter 5.

4.4 After the Cuts

We have investigated a number of selection criteria, with emphasis on optimising continuum suppression. In the next chapter, we will finally measure the recoil mass of π_1, by fitting data points to a function. The mean of this function will give us the mass of Z_b^+ and we will compare these values across selection criteria and Phase. Before doing so, we summarise the selection criteria and the selection efficiencies in Figure 4.24 below.

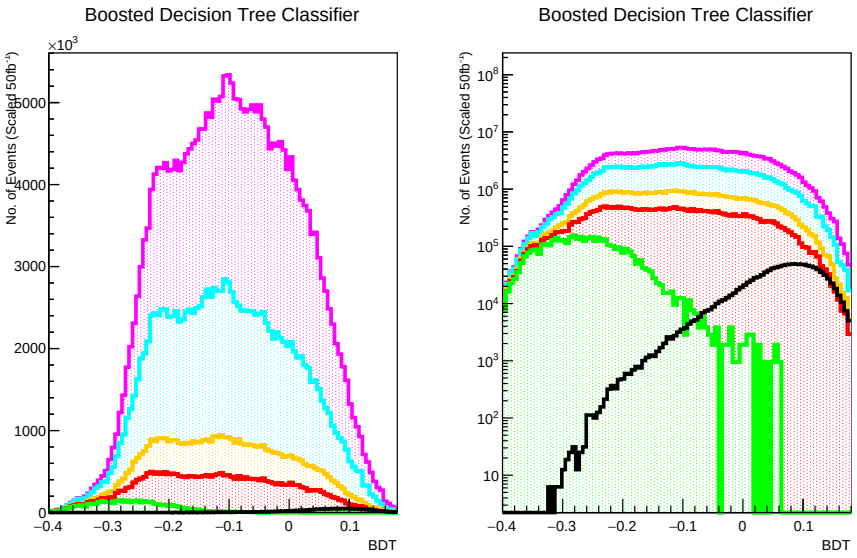

Figure 4.18: Phase II Classifier Distribution.

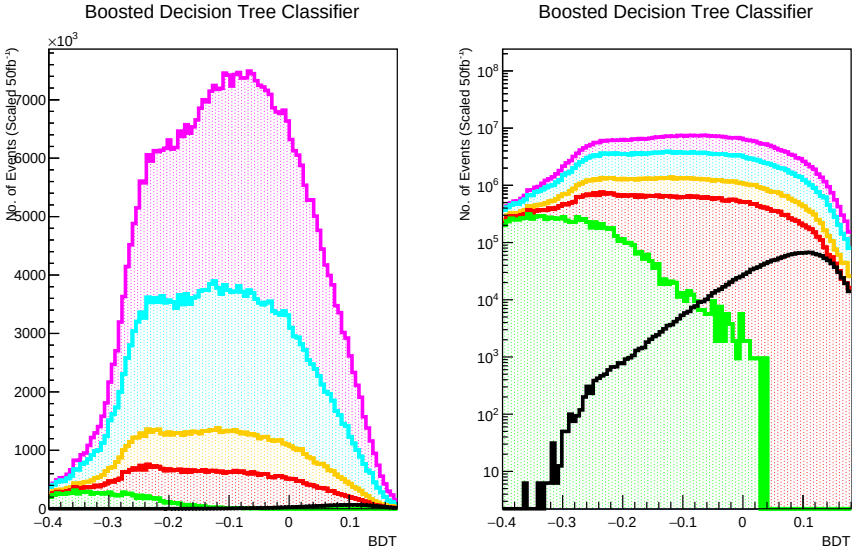

Figure 4.19: Phase III Classifier Distribution.

	Continuum Suppression Variables	Separation
R_2	Reduced Fox-Wolfram Moment, the ratio between momenta of jet-like events and momenta of spherical events	0.3477
ThrustO	Magnitude of non-B products thrust axis.	0.3266
cc9	CleoCone9, sum of momenta of non-B products with ThrustO axis directed between 80 to 90°of B-meson axis	0.1169
et	Transverse energy	0.1101
cc8	CleoCone8, sum of momenta of non-B products with ThrustO axis directed between 70 to 80°of ThrustB axis	0.09821
hoo4	Modified Fox-Wolfram Moment	0.09809
hso02	Modified Fox-Wolfram moment	0.067
hso12	Modified Fox-Wolfram moment	0.0543
hso10	Modified Fox-Wolfram moments	0.0534
CostTBTO	Cosine of angle between ThrustB axis and ThrustO axis.	0.0513
hoo0	Modified Fox-Wolfram moment	0.0498
hso00	Modified Fox-Wolfram moment	0.045
hoo1	Modified Fox-Wolfram moment	0.0322
hso20	Modified Fox-Wolfram moment	0.0302
hoo3	Modified Fox-Wolfram moment	0.0295
hso22	Modified Fox-Wolfram moment	0.0283
hso04	Modified Fox-Wolfram moment	0.0237
hso14	Modified Fox-Wolfram moment	0.0169
hso24	Modified Fox-Wolfram moment	0.01556
ThrustB	Magnitude of B meson thrust	0.01235
hso03	Modified Fox-Wolfram moment	0.009737
hso01	Modified Fox-Wolfram moment	0.008926
CosTBz	Cosine of the angle between B meson axis and z-axis	0.005718

Figure 4.20: List of Continuum Suppression Variables implemented in our analysis. As a SuperB factory, these Belle II variables are defined assuming that processes occur as $\Upsilon(4S) \rightarrow B\bar{B}[?]$. In our $\Upsilon(6S) \rightarrow Z_b^+\pi^-$, we saw in the phase space diagram of Figure 3.5 that the π_1 event was spherical. As the B mesons are roughly spherical as well, we could consider these definitions as referring to π_1 in our case.

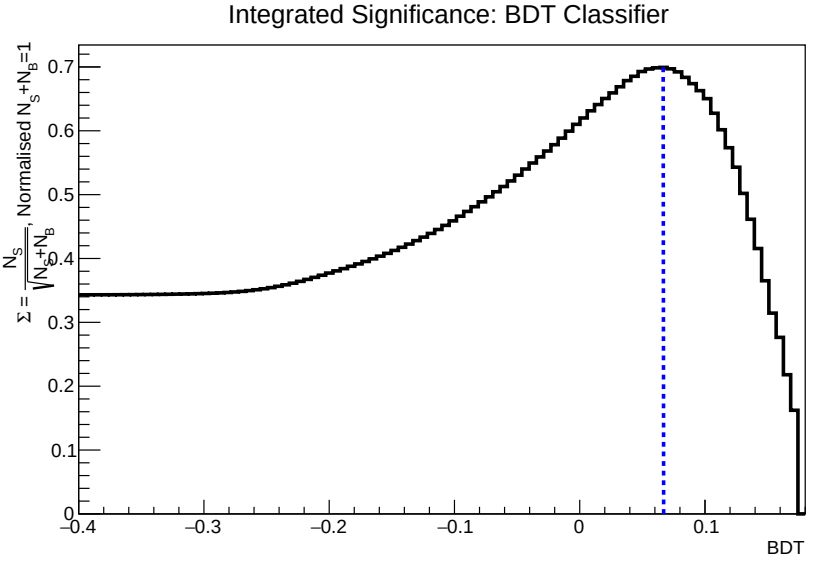

Figure 4.21: Figure of Merit Phase II: The integrated significance is evaluated for subsets of pions with BDT classifier between b and 1, where b values are BDT cut values, on the x axis. The blue dotted line corresponds to the cut BDT <0.0669, which gives the maximum significance in both Phase II and Phase III.

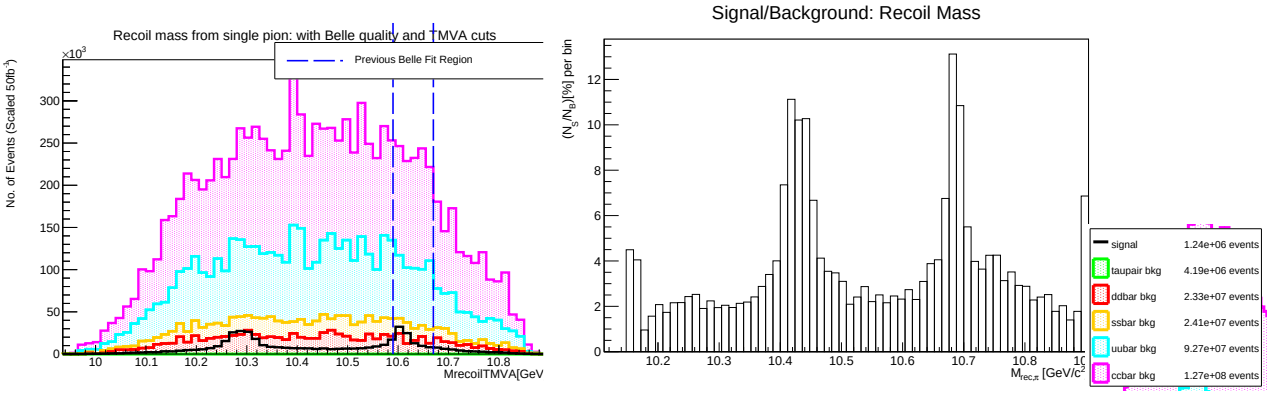

Figure 4.22: Phase II, after quality cuts and BDT cut .

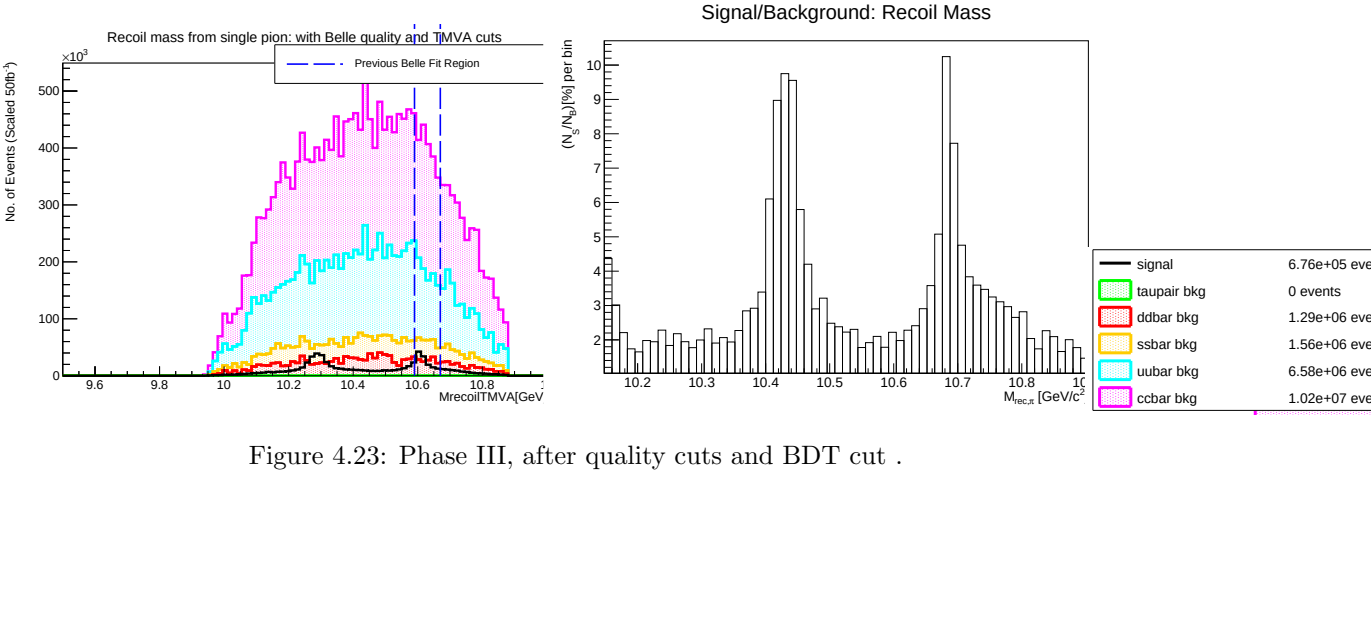

Figure 4.23: Phase III, after quality cuts and BDT cut .

Phase	*Process*	*No. of π(initial)*	*No. of π(after quality cuts)*	*% retained*	*No. of π(after quality and R2 cuts)*	*% retained*
II	$c\bar{c}$	1.27×10^8	6.71×10^7	52.89	4×10^7	31.51
II	$d\bar{d}$	2.33×10^7	1.27×10^7	54.67	7.14×10^6	30.68
II	$s\bar{s}$	2.41×10^7	1.18×10^7	48.89	6.56×10^6	27.24
II	$\tau^+\tau^-$	4.2×10^6	2.1×10^6	49.97	2.96×10^5	7.04
II	$u\bar{u}$	9.27×10^7	5.1×10^7	55.04	2.78×10^7	29.98
II	All Continuum	2.71×10^8	1.45×10^8	53.38	8.18×10^7	30.16
II	Signal	1.25×10^6	7.94×10^5	63.56	7.7×10^5	61.66
III	$c\bar{c}$	2.02×10^8	1.08×10^8	53.66	6.91×10^7	34.19
III	$d\bar{d}$	3.69×10^7	2.05×10^7	55.54	1.21×10^7	32.86
III	$s\bar{s}$	4.11×10^7	2.04×10^7	49.51	1.22×10^7	29.55
III	$\tau^+\tau^-$	1.01×10^7	4.87×10^6	48.33	7.49×10^5	7.43
III	$u\bar{u}$	1.48×10^8	8.1×10^7	54.85	4.74×10^7	32.08
III	All Continuum	4.38×10^8	2.35×10^8	53.70	1.42×10^8	32.31
III	Signal	1.79×10^6	1.14×10^6	64.05	1.12×10^6	62.44

Phase	*Process*	*No. of π(after quality and optimised R2 cuts)*	*% retained*	*No. of π(after quality and BDT cuts)*	*% retained*
II	$c\bar{c}$	1.22×10^7	9.65	5.55×10^6	4.38
II	$d\bar{d}$	2.09×10^6	8.99	8.76×10^5	3.77
II	$s\bar{s}$	2.05×10^6	8.52	7.97×10^5	3.31
II	$\tau^+\tau^-$	5.28×10^4	1.26	0	0
II	$u\bar{u}$	8.32×10^6	8.98	3.35×10^6	3.62
II	All Continuum	2.48×10^7	9.13	1.06×10^7	3.9
II	Signal	5.27×10^5	42.17	4.4×10^5	35.21
III	$c\bar{c}$	2.2×10^7	10.86	1.02×10^7	5.04
III	$d\bar{d}$	3.75×10^6	10.14	1.29×10^6	3.49
III	$s\bar{s}$	3.90×10^6	9.48	1.56×10^6	3.79
III	$\tau^+\tau^-$	1.14×10^5	1.13	0	0
III	$u\bar{u}$	1.47×10^7	9.96	6.58×10^6	4.46
III	All Continuum	4.44×10^7	10.14	1.96×10^7	4.48
III	Signal	7.83×10^5	43.84	6.76×10^5	37.84

Figure 4.24: Selection efficiencies for varying combinations of continuum suppression criteria

Chapter 5

Fitting the Results

We have successfully applied selection criteria to our signal and background MC, with the intention of reducing the number of background pions that are misidentified as other final state particles, as well as those that originate from beam-induced events or continuum events. These criterion have rejected background pions whilst preserving the number of signal pions that will contribute to our measurement of the Z_b^+ mass. To continue towards this measurement, we fit the recoil mass distributions from signal MC and background MC with probability density function hypotheses. The fit parameters derived can then be implemented in future true $\Upsilon(6S)$ collision data, to see if the data is consistent with the presence of Z_b^+ described by our signal MC. To perform our fits, we will use the `Roofit`, a further toolkit for data modelling in `ROOT`.

In Chapter 4, we applied the Belle selection criteria with three different continuum suppression conditions to the signal and background recoil mass distributions: the original Belle condition R2 <0.3, the max integrated significance condition R2 <0.135 and the TMVA classifier condition of relevant continuum suppression variables, $\pi-$BDT <0.0669. All three cases will be fit, so that we can consider the parameters of each probability density function, as a measure to identify the best selection criteria combination.

5.1 Fitting the Signal MC

Recalling the method of fitting used in the 2016 Belle analysis, as explained in Chapter 1, we have chosen to go an alternate route. We implemented the 9.8 GeV/c^2 $<M_{rec,\pi^+\pi^-}$ 10.0 GeV/c^2 as a preselection requirement on our dipion pairs, so we are not able to to fit the $M_{rec,\pi^+\pi^-}$ resonance for ranges of $M_{rec,\pi}$. As an MC analysis, we have distinct pion samples from background MC and signal MC, so we will instead fitting those separately.

We fit the single pion recoil mass of our signal MC as the convulution of two probability density functions: the sum of two Gaussians, for the π_1 and π_2 peak and a Chebychev polynomial, which was implemented in the 2016 Belle analysis to fit combinatoric background. The Chebychev polynomial ifit is the most precarious contribution to the overall fit, as we have a choice polynomial degree. `RooFit` only supports up to 6th degree Chebychev polynomials, so we vary the degree for each fit, to choose the degree that minimises the χ^2 degrees of freedom. The table in Figure 5.1 demonstrates that χ^2 is consistently smaller for the BDT continuum cuts than both R2 cuts, across the same degree fit. It should be noted that the 2016 Belle analysis used fourth order Chebychev polynomials for their fits —whether it is signifiant that we have signal fits to third, fifth and sixth order is unknown. We have demonstrated that not only does using TMVA methods to consider most continuum suppression variables maximise the signal-to-background ratio, but we have seen here that the signal MC itself is better fit with this cut. It's only short coming is that it has the largest statistical error, σ —but not not by much!

Phase	*Chebychev degree*	χ^2 *for BDT >0.0669*	χ^2 *for R2 <0.135*	χ^2 *R2 <0.3*
II	2	31.8425	65.3616	92.2159
II	3	21.6834	41.5388	64.4064
II	4	24.7557	42.8642	66.3386
II	5	**21.60037**	**32.8447**	51.2359
II	6	32.1625	33.2541	**50.3752**
III	2	28.5728	53.9344	80.7305
III	3	**28.3198**	48.5941	69.9644
III	4	31.8065	48.6058	70.1881
III	5	41.6767	**48.5068**	**69.1766**
III	6	68.4764	56.2377	81.6745

Figure 5.1: χ^2 values for signal MC pion recoil mass fit. The coefficients of the Chebychev polynomial of the given degree is calculated such that the convolution of the polynomial and the Gaussians that fit the π_1 and π_2 peaks parameterise the full distribution. We begin with quadratic degree due to the concavity of the combinatoric background. Final fits are indicated in bold.

5.2 Fitting the Background MC

For completeness, we fit the background MC, for future use in real data. Chebychev polynomials are used again, this time used as the sole function to fit the continuum contribution to the recoil mass. We proceed in the same way as before; vary the degree of the Chebychev polynomial to examine which degree minimises the χ^2 fit value.

A number of fits failed to converge meaningfully, mostly in Phase II for R2 <0.3 . The reason for this remains unknown.

5.3 Systematic Errors

The design of this analysis is not perfect. We consider some places for improvement below.

- A number of R2 <0.3 fits failed. The fit quality could be improved by fitting beam background-free MC, then forcing these parameters to the distribution with beam background. A further Chebychev polynomial could be implemented to quantify the beam background contribution, which may "smooth" discontinuous points that struggle to be fit.
- Further MC campagins have occured since this analysis took place, meaning larger data samples of $\Upsilon(6S)$ decays are available. The effect of limited statistics, especially with the need to have statistically independent testing and training samples for the TMVA process, that led to discontinuous peaks could be minimized.
- We opted to use the $h_b(1P)$ mass as preselection criteria, to fit the Z_b^+ distribution. As we based our work from the 2016 analysis, a further activity could be to compare the efficacy of both methods.

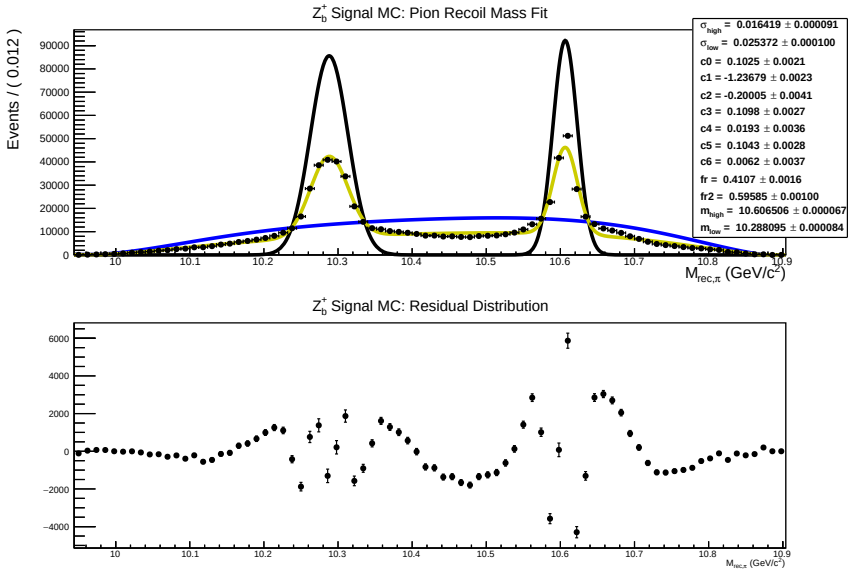

(a) R2 <0.3

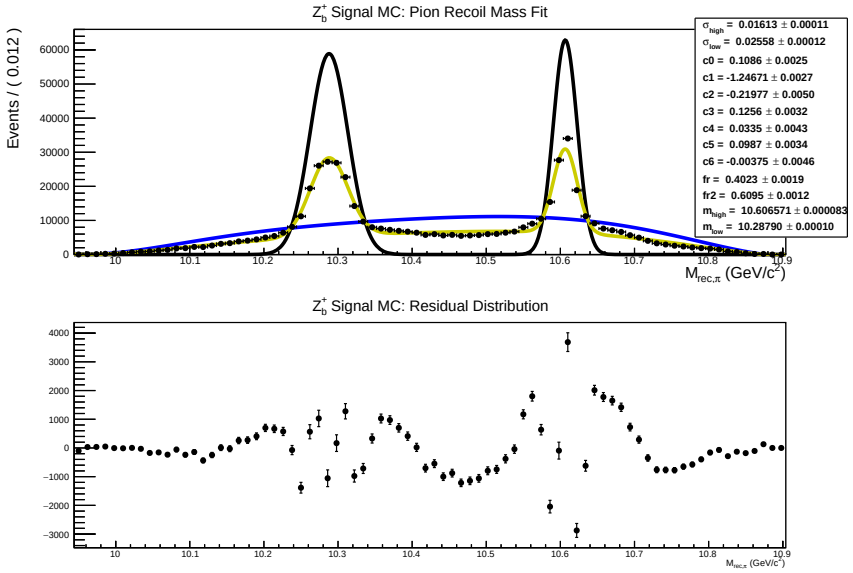

(b) R2 <0.135

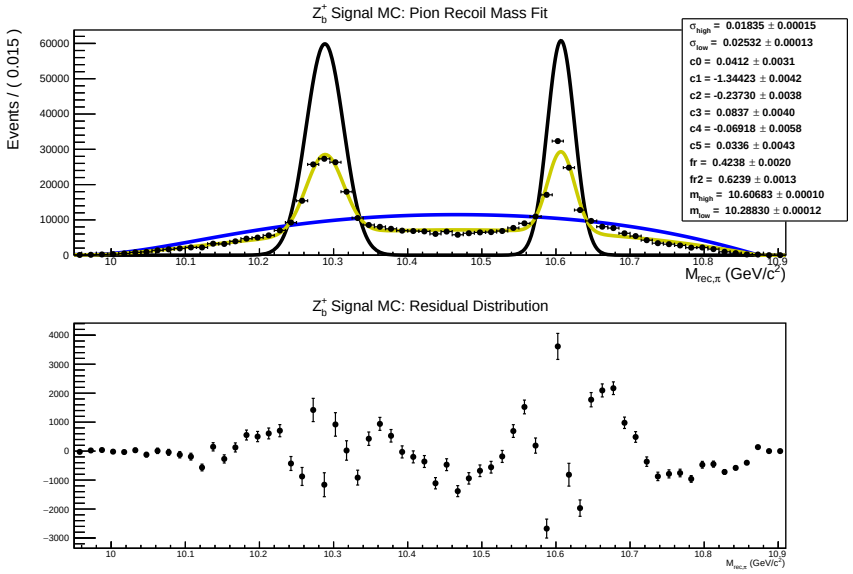

(c) BDT >0.0669

Figure 5.2: Phase II Signal Fitting (gold line). The amplitudes of the double Gaussian (black line) and Chebychev polynomial (blue line) are exaggerated for visibility. Chebychev polynomial coefficients are denoted in the box above

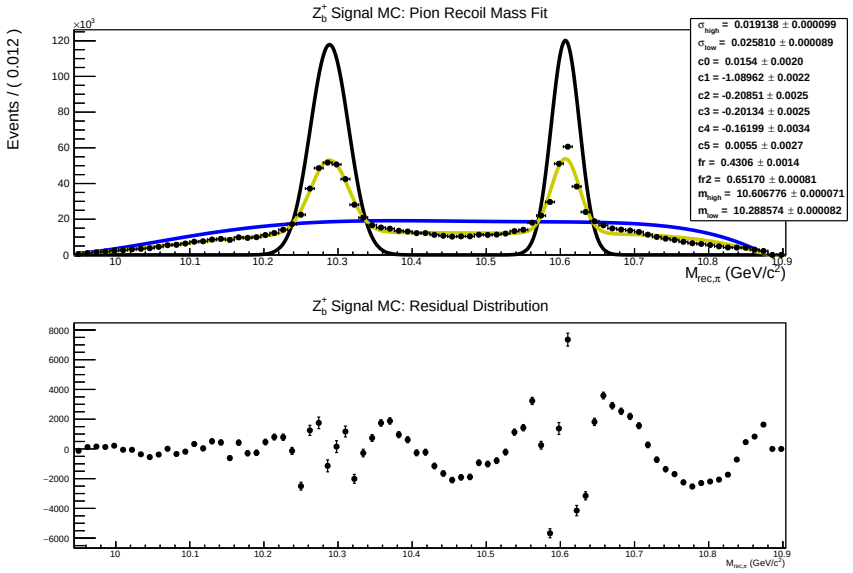

(a) R2 <0.3

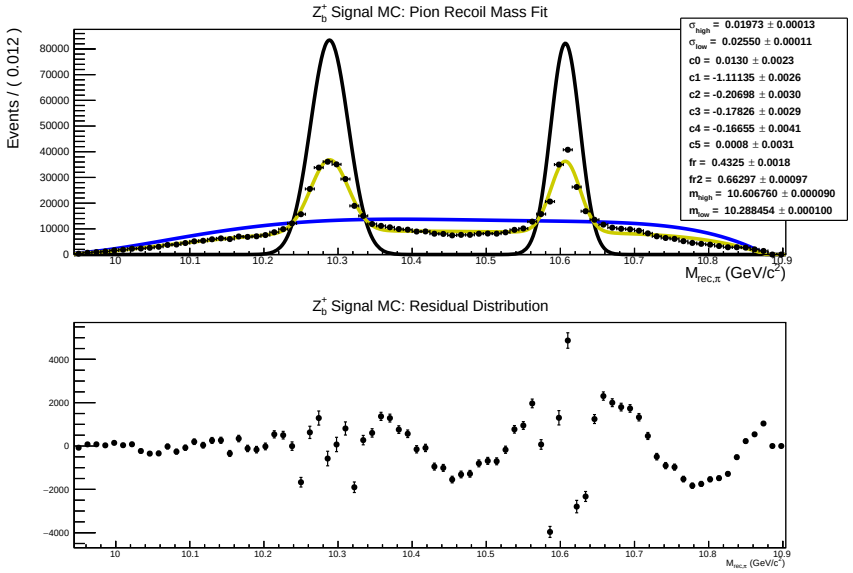

(b) R2 <0.135

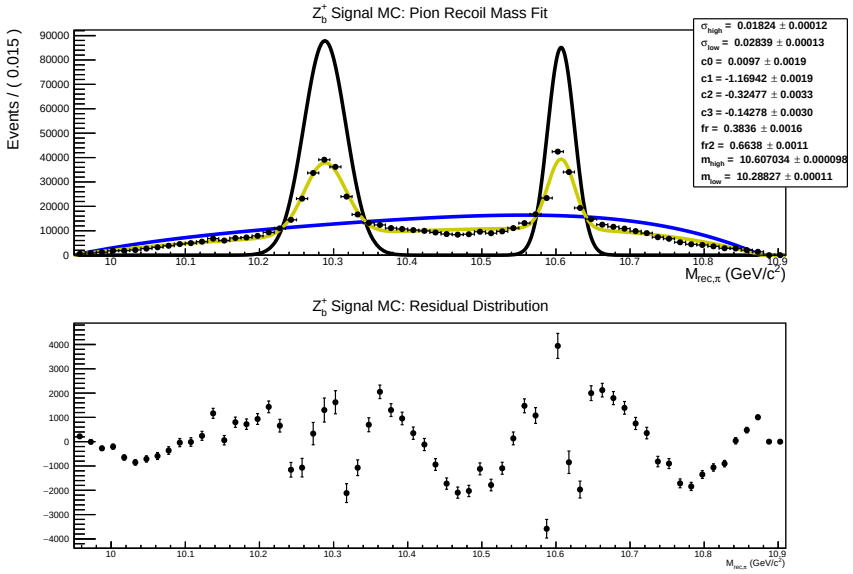

(c) BDT >0.0669

Figure 5.3: Phase III Signal Fitting (gold line). The amplitudes of the double Gaussian (black line) and Chebychev polynomial (blue line) are exaggerated for visibility

Phase	*Chebychev degree*	χ^2 *for BDT >0.0669*	χ^2 *for R2 <0.135*	χ^2 *R2 <0.3*
II	2	3.51029	13.3612	failed
II	3	1.88154	6.34208	failed
II	4	1.670827	4.10372	failed
II	5	1.60895	3.35567	failed
II	6	1.52621	3.33982	failed
III	2	1.58336	failed	failed
III	3	1.58525	3.24757	failed
III	4	1.57734	3.10684	7.33823
III	5	1.3391	2.08196	5.06741
III	6	**1.3294**	**1.95905**	**4.4392**

Figure 5.4: χ^2 values for background MC pion recoil mass fit. The coefficients of the Chebychev polynomial parameterise the full background distribution. We begin with quadratic degree due to the concavity of the combinatoric background. Final fits are indicated in bold.

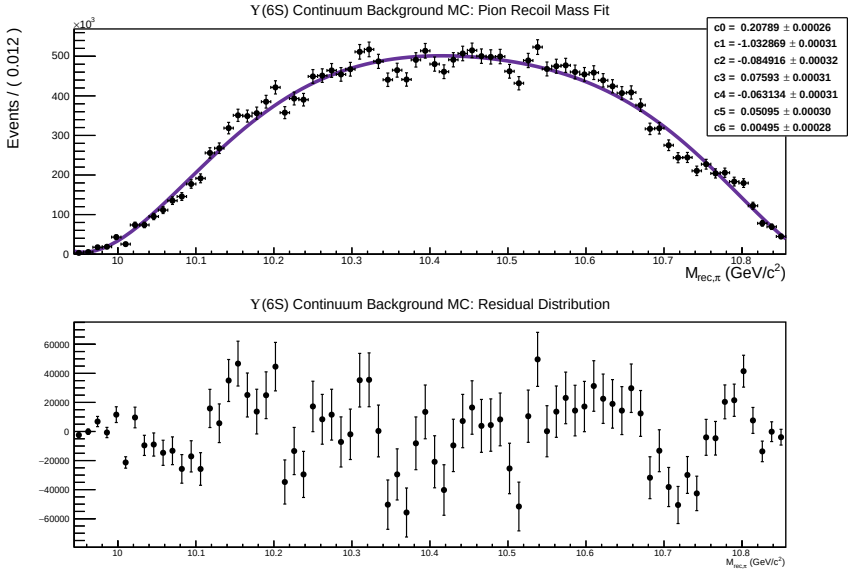

(a) R2 <0.135

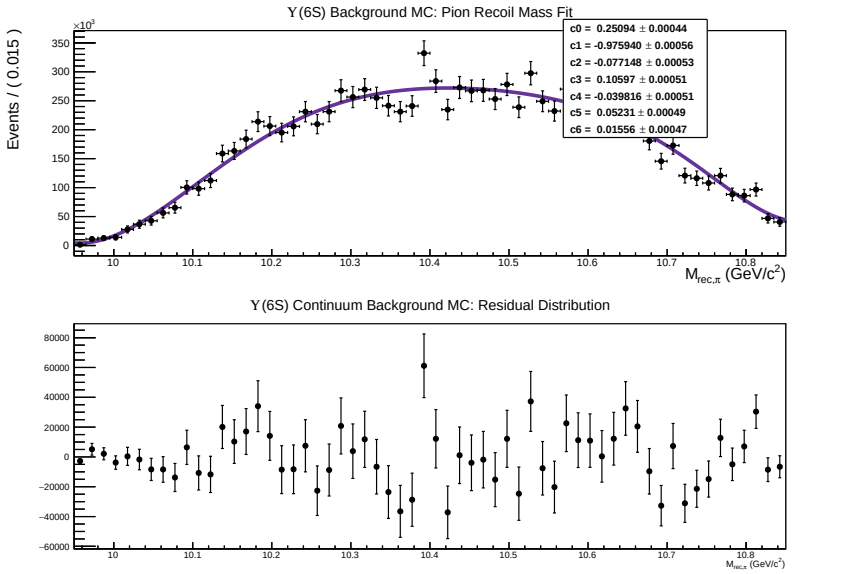

(b) BDT >0.0669

Figure 5.5: Phase II Background Fitting (purple line). The R2 <0.3 background was unable to be fit.

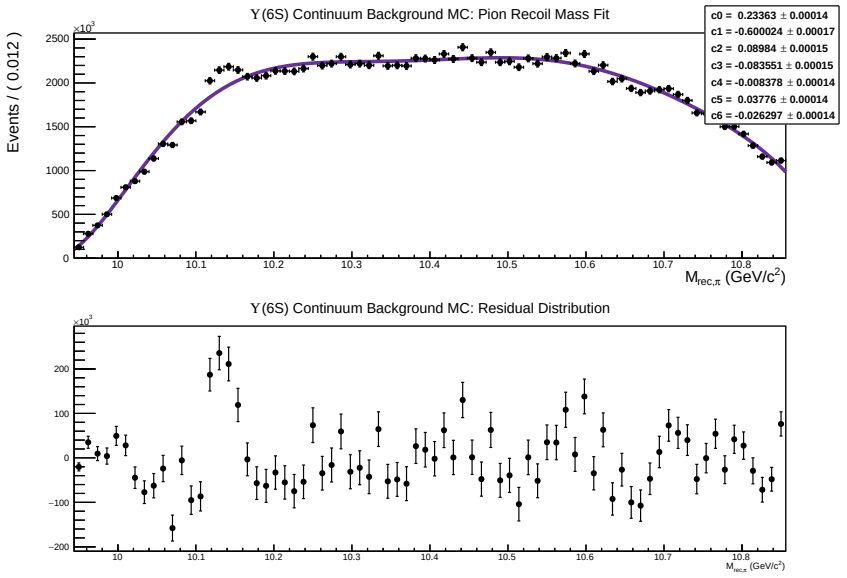

(a)

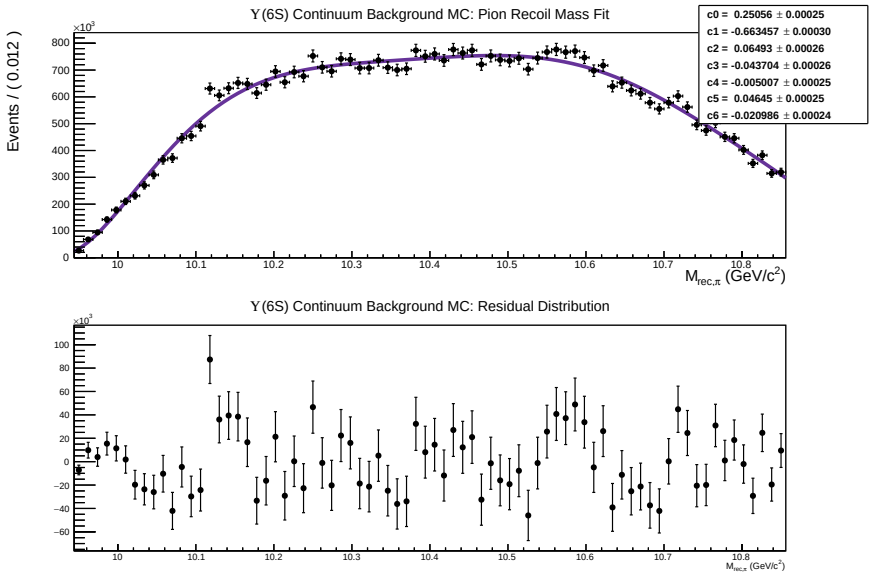

(b)

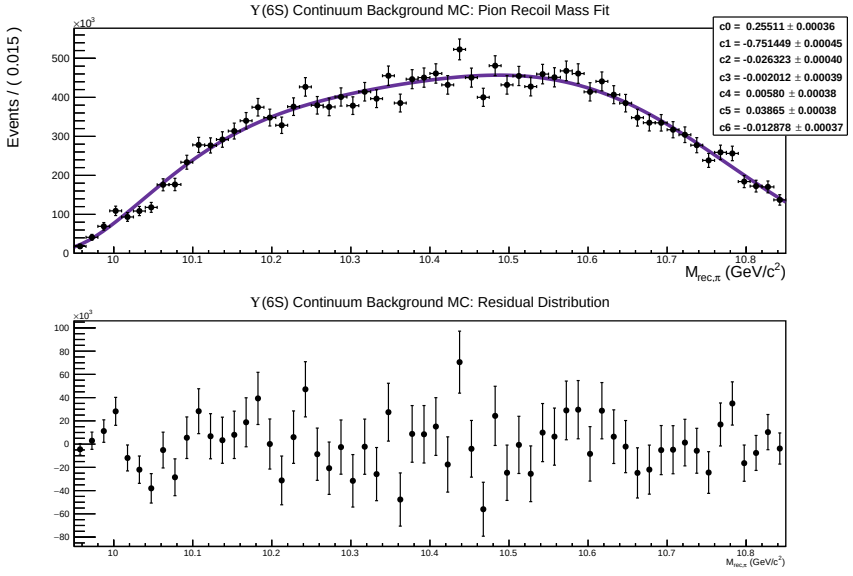

(c)

Figure 5.6: Phase III Background Fitting (purple line).

Chapter 6

The Future: To $qq\bar{q}\bar{q}$ and Beyond

Our analysis is complete. We have found the following values for Z_b^+ mass fitted from the recoil mass of pions found in $\Upsilon(6S)$ decays of Belle II MC. Unsurprisingly, the Phase III fit after implementing the BDT classifier selection criteria was the closest to matching the mass 10.6072 GeV/c^2 dictated by the decay tables. However, all selection criteria were within error of this mass. We have thus demonstrated that Phase II has potential in an exotic hadron search, despite lacking in vertexing and operating with diminished tracking efficiency, can gather just as significant data as in Phase III.

Phase II

$M_{rec,\pi,R2<0.3} = (10.606506 \pm 0.000067)$ GeV/c^2 $\sigma_{R2<0.3} = 0.016419\pm$ 0.000091
$M_{rec,\pi,R2<0.135} = (10.606571 \pm 0.000083)$ GeV/c^2 $\sigma_{R2<0.133} = 0.01613\pm$ 0.00011
$M_{rec,\pi,BDT>0.0669} = (10.60683 \pm 0.0001)$ GeV/c^2 $\sigma_{\pi,BDT>0.0669} = 0.01835\pm$ 0.00015

Phase III

$M_{rec,\pi,R2<0.3} = (10.606776 \pm 0.000071)$ GeV/c^2, $\sigma_{R2<0.3} = 0.019138\pm$ 0.000099
$M_{rec,\pi,R2<0.135} = (10.606760 \pm 0.000090)$ GeV/c^2, $\sigma_{R2<0.135} = 0.01973\pm$ 0.00013
$M_{rec,\pi,BDT>0.0669} = (10.60734 \pm 0.000098)$ GeV/c^2, $\sigma_{\pi,BDT>0.0669} = 0.01824\pm$ 0.00012

The search for Z_b^+, however, is just about to begin. We have the parameters of our fits prepared, ready to apply to true collision data and to measure the agreement with the presence of Z_b^+. We found that All we await now is successful completion of the technical upgrade, so as to start looking for hints of Z_b^+. With the 10 year lifespan of the previous experiment, we can only hope that a Belle II exotic discovery happens within the decade. In the meantime, we have the option of using our new found TMVA methods to return to the original Belle data set used in 2016, to see if this analysis can extract further significance than what was previously documented.

Pursuing exotic mesons and exotic baryons is an exciting field; it challenges some of the first assumptions one learns as a particle physicist, that mesons are $q\bar{q}$ and baryons are qqq. The possibilities, so far, seem endless; why stop at just 4 quark mesons? Why not 6, 8, 10 quark groupings?! It is this "Dr. Frankenstein"-esque hadron building that led me to become an aspriring experimental particle physicist. I have thoroughly enjoyed developing an intuition for detector phenomenology as a Belle II analyst and I hope to continue this work in exotica at Belle II in higher research degrees and beyond.

Bibliography

[1] G Zweig. An SU_3 model for strong interaction symmetry and its breaking; Version 1. Technical Report CERN-TH-401, CERN, Geneva, Jan 1964.

[2] M. Gell-Mann. A schematic model of baryons and mesons. *Physics Letters*, 8(3):214 – 215, 1964.

[3] C. Patrignani et al. Quarks: Review of Particle Physics. *Chin. Phys.*, C40(10):100001, 2016.

[4] Angelo Esposito, Andrea L. Guerrieri, Fulvio Piccinini, Alessandro Pilloni, and Antonio D. Polosa. Four-Quark Hadrons: an Updated Review. *Int. J. Mod. Phys.*, A30:1530002, 2015.

[5] L. Maiani, F. Piccinini, A. D. Polosa, and V. Riquer. A New look at scalar mesons. *Phys. Rev. Lett.*, 93:212002, 2004.

[6] Roel Aaij et al. Observation of the resonant character of the $Z(4430)^-$ state. *Phys. Rev. Lett.*, 112(22):222002, 2014.

[7] I. Adachi et al. Study of Three-Body Y(10860) Decays. 2012.

[8] M. Dugger et al. A study of meson and baryon decays to strange nal states with GlueX in Hall D. 2012.

[9] R. Aaij et al. Evidence for exotic hadron contributions to $\Lambda_b^0 \to j/\psi p\pi^-$ decays. *Phys. Rev. Lett.*, 117:082003, Aug 2016.

[10] R. Aaij et al. Model-independent evidence for $j/\psi p$ contributions to $\Lambda_b^0 \to j/\psi pK^-$ decays. *Phys. Rev. Lett.*, 117:082002, Aug 2016.

[11] Kazuo Abe et al. Observation of a new narrow charmonium state in exclusive B+- —¿ K+- pi+ pi- J / psi decays. In *Proceedings, 21st International Symposium on Lepton and Photon Interactions at High Energies (LP 03): Batavia, ILL, August 11-16, 2003*, 2003.

[12] A. Bondar et al. Observation of two charged bottomonium-like resonances in Y(5S) decays. *Phys. Rev. Lett.*, 108:122001, 2012.

[13] A. Abdesselam et al. Energy scan of the $e^+e^- \to h_b(nP)\pi^+\pi^-$ $(n = 1, 2)$ cross sections and evidence for $\Upsilon(11020)$ decays into charged bottomonium-like states. *Phys. Rev. Lett.*, 117(14):142001, 2016.

[14] T. Abe et al. Belle II Technical Design Report. 2010.

[15] S. Hashimoto et al. Letter of intent for kek super b factory. Report Part 1: Physics, Belle, 2004.

[16] J. Haba et al. Letter of intent for kek super b factory. Report Part 2: Detector, Belle, 2004.

[17] J.W. Flanagan et al. Letter of intent for kek super b factory. Report Part 3: Accelerator Design, Belle, 2004.

[18] Torben Ferber and Phillip Urquijo. Overview of the belle ii physics generators. Jun 2015.

[19] Andreas Hocker et al. TMVA - Toolkit for Multivariate Data Analysis. *PoS*, ACAT:040, 2007.

[20] David J. Gross and Frank Wilczek. Ultraviolet behavior of non-abelian gauge theories. *Phys. Rev. Lett.*, 30:1343–1346, Jun 1973.

[21] H. David Politzer. Reliable perturbative results for strong interactions? *Phys. Rev. Lett.*, 30:1346–1349, Jun 1973.

[22] N. Brambilla et al. Heavy quarkonium: progress, puzzles, and opportunities. *Eur. Phys. J.*, C71:1534, 2011.

[23] M. B. Voloshin. Charmonium. *Prog. Part. Nucl. Phys.*, 61:455–511, 2008.

[24] N. Brambilla et al. QCD and Strongly Coupled Gauge Theories: Challenges and Perspectives. *Eur. Phys. J.*, C74(10):2981, 2014.

[25] Jun John Sakurai and Eugene D Commins. Modern quantum mechanics, revised edition, 1995.

[26] A. J. Bevan et al. The Physics of the B Factories. *Eur. Phys. J.*, C74:3026, 2014.